

## IMPACT TEST OF SURFACE

**ANTONÍN KŘÍŽ<sup>a\*</sup>, PETR BENEŠ<sup>b</sup>,  
and JIŘÍ ŠIMEČEK<sup>b</sup>**

<sup>a</sup> Research Centre of Rail Vehicles, <sup>b</sup> Department of Material Science and Technology, Faculty of Mechanical Engineering, University of West Bohemia, Plzeň, Czech Republic  
kriz@kmm.zcu.cz

Keywords: Impact tester, Rail Vehicle Wheel Materials

### 1. Introduction

In numerous industrial applications, machine parts are subjected to high contact load. Mechanical interaction of two surfaces results in such conditions, which may lead to their degradation. Such damage is usually the limiting factor of their service life. This is why methods for elimination or at least controlling such degradation are sought<sup>1</sup>.

One of available techniques for investigation of contact degradation is impact testing. With an impact tester it is possible to determine the response of materials to dynamic impact contact wear. The resistance to impact contact load can be examined not only in bulk materials but also in surface-treated materials. Another type of test, which can be run on the impact tester, is investigation of contact impact fatigue. Contact impact fatigue is an important material parameter, as it controls the initiation of fatigue cracks throughout the volume of the piece, which eventually results in the machine part failure<sup>2,3</sup>.

### 2. Impact Tester Designs

The impact force is not exerted through the free fall of the indenter but by magnetic force generated by an electromagnetic coil. The arm in this type of impact tester is actuated by a coil, which exerts the required force. The indenter is mounted on the arm. The holder with the indenter is returned to their initial position by a spring force. The test piece is mounted on a rotating and extending stage. Owing to the guiding mechanism of the stage, it is possible to arrange the impact sites in a straight line, which is beneficial for some types of measurements. In order to apply the load at other angles, the stage can be modified by adding a positioning device. This type of impact tester will be extended in near future with additional measuring equipment (for accelerometric and acoustic emission measurements). These modifications will significantly expand its application potential.

Dynamic contact wear does not rank among the basic wear modes. It is a combination of mechanisms involving adhesive, abrasive, fatigue and vibration wear. With impact test it is possible to determine the contact fatigue strength of selected materials. Testing based on scratch-test techniques (progressive penetration of a stylus into surface under increasing load) or tribological procedures might be inadequate for simulation of conditions, where the surface of material is subjected to both fatigue load and erosive wear. The impact test is a more accurate simulation of a real-world situation affecting the service-life of material (e.g. "pulsating" contact between the cutting tool and work piece due to vibrations).

### 3. The Use of Impact Testing for Rail Vehicle Wheel Materials

One of important areas of application of impact test is measurement of impact fatigue life of rail vehicle wheels. In this case, the instrument was used for bulk material. The advantage of investigation of impact fatigue life of rail vehicle wheel materials with the impact tester lies in the fact that the simulation of the wheel load is very similar to the real-world application conditions. The impact load acts on the wheel surface when it rolls across railway turnouts, joints or expansion gaps. In all these cases, the wheel surface is subjected to dynamic impacts. This might induce a particular type of response of material and cause damage, such as formation of cracks, defects, etc. Since presence of cracks in a rail vehicle wheel is undesirable, formation and propagation of cracks due to impact fatigue load requires great attention.

Cracks may form due to various factors and in different ways. Each of crack formation modes is specific to the given material and, particularly, to its internal structure. It cannot be thought of as applicable to other types of materials. This indicates the importance of investigation of mechanisms, which take place in the material as a result of contact fatigue loads. Dynamic loading of wheels in operation can be most accurately simulated with an impact tester, which outperforms any other laboratory testing methods in this respect.

The microstructure of the material in question consisted of ferrite and pearlite and some areas of Widmannstätten-type microstructure. The presence of the Widmannstätten microstructure might have an adverse effect on mechanical properties of steel and might lead to premature crack formation. Impact testing provided no evidence of the Widmannstätten microstructure being the initiation site for cracks. The indenter was a 6 mm diameter tungsten carbide ball. Thanks to its hardness, this material shows excellent resistance to dynamic contact load, which makes

it an ideal candidate for impact testing. In order to clarify the damage mechanism and to capture the progressive wear of the specimen surface and the formation of impact sites, various numbers of impacts were used for the test: 500; 1000; 2500; 5000; 10 000 and 100 000. The rail vehicle wheels were tested with the indenter impact energy of  $E = 0.078 \text{ J}$ .

After as few as 500 impacts, numerous defects were observed in the fringe area of the impact site. In some locations, these defects coalesced, which gave rise to continuous bands of cavities. The concentration of the bulk of defects in the fringe area of the impact site is related to the distribution of the tensile stress, which reach their peak in this location. As a result, cracks and defects form in this area and may coalesce. On the contrary, the prevailing type of stress in the impact site centre is the compressive stress. Even the initial surface showed numerous defects. It is therefore likely that the resulting defects did not form during the impact but, instead, were present on the specimen surface and grew or coalesced due to impact-induced surface and subsurface stresses. Microscopic observation of the centre of the 500-impact impact site did not reveal any defects. However, they might have been closed by the forging action of the indenter.

After 1000 impacts, the fringe area of the impact site showed a network of fine cracks. Propagation of cracks into other areas than the impact site was not detected. Those fringe areas, where no cracks were found, showed defects, same as the specimen upon 500 impacts.

With the growing number of impacts, the number of defects in the fringe areas of the impact site was decreasing. By contrast, the number of defects in the centre of the impact site was increasing.

Upon 100 000 impacts, it was found that the source of hairline cracks are the defects in the fringe areas of the impact site (Fig. 2). This finding suggests that the material responds to high-cycle impact fatigue load by forming microscopic cracks. One can assume that upon increasing the number of impacts, these hairline cracks would propagate further and serious damage of the material would occur. It is impossible to verify this hypothesis using the existing low-frequency impact tester, as the high-cycle

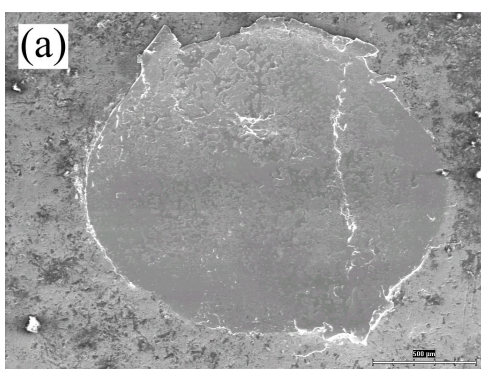


Fig. 1. Impact site upon 100 000 impacts

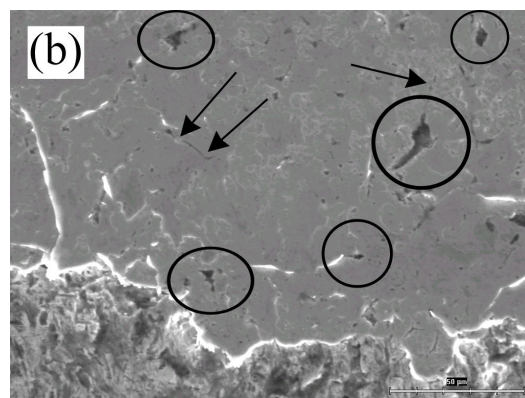


Fig. 2. Detailed view of the impact site (Fig. 1) fringe area; clusters of defects (marked with a circle), hairline cracks (marked with an arrow)

testing (above 100 000 impacts) would be very time-consuming.

The crack, which had been revealed during machining of the specimen (Fig. 3a,b), propagated rapidly in the course of the 100 000-impact loading cycle. The crack was outside the impact site. Since the crack propagated from the area of specimen, which was under the clamping flange that held the specimen in the testing instrument, it can be assumed that the crack propagation was due to the propagation of the impact load throughout the whole volume of material. The shock waves emanate from the impact site and reach all parts of the material. The shock wave energy reduces the critical stress for the crack growth. As a result, the crack easily enters the sound material outside the impact site. Moreover, fastening the specimen with a flange introduces further stresses in the material. Those become another factor promoting the propagation of existing cracks outside the impact site. More cracks were found in the neighbourhood of the crack in question (Fig. 3b). It was not established whether these cracks were formed as a results of the impact loading.

It is evident that propagation of cracks existing in the material can be induced by impact energy introduced by a blow of the indenter on the specimen surface and reaching the crack tip.

#### 4. Development of Impact Tester and the Testing Procedure

Defects produced by contact loading are often so minute that they cannot be observed without light or scanning electron microscopes. Therefore, investigation methods must be very accurate in order to capture initiated changes even at time of testing. For this reason, acoustic emission signal is recorded over the course of the impact test and provides an indication of significant crack propagation. Another useful feature of the instrument is a strain

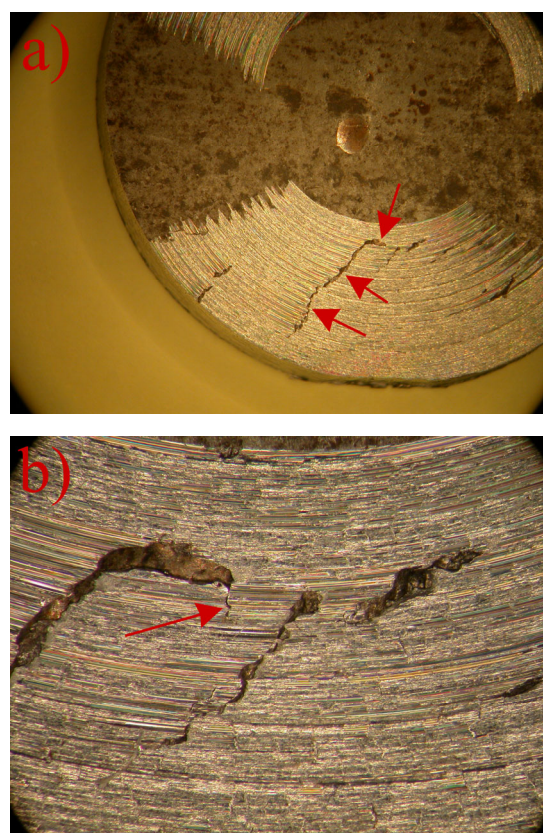


Fig. 3. (a) A crack outside the impact site - the crack was growing during the impact test, (b) detail of the crack end, where further propagation in the form of a hairline crack is visible

gauge. It measures the individual impact force for the purpose of verification of the equipment settings and also reveals the signs of hardening and softening processes. With such data it is possible to identify the key moment of the contact loading process. The hardening process, i.e. formation of dislocation pile-ups in slip systems, leads to propagation of cracks during the period of further loading. Combining the outputs of both instruments can reveal the degradation processes – which play a crucial role in contact loading – at an early stage.

Fig. 4 shows further planned design modifications. Fixtures for multi-axis loading and bending on a mandrel are being manufactured. With this design modification, more faithful simulation of complex loading conditions will be available. These design modifications are particularly important in testing of bulk materials where the initial crack is often closing due to a compressive load. Where the part operates under tensile load, rapid degradation takes place. This often occurs in practice but it could not have been simulated on the basis of tests under simple loading conditions performed thus far.

Further design modifications also stem from practical requirements. Testing of railway wheels and materials for

rails requires the presence of a liquid, which significantly alters the stress effects. A special chamber will be designed to provide required temperatures and environments and to allow exploration of effects of climatic and thermal conditions on properties of materials and on development of degradation processes.

These new design solutions will entail fine-tuning of current testing methods. Current testing conditions typically include low loading forces and a high number of cycles. With these settings, individual changes taking place in the material can be detected accurately. Images of the impact crater were captured with a light microscope, scanning electron microscope and a laser scanning confocal microscope. Their evaluation focused not only on formed local defects (their size is often on the order of micrometers) but also on the magnitude of plastic deformation. New methods are being developed, which rely on measurement of residual stresses in the impact crater area and its surroundings. The measurement must be performed immediately upon the exposure, which is why a simple

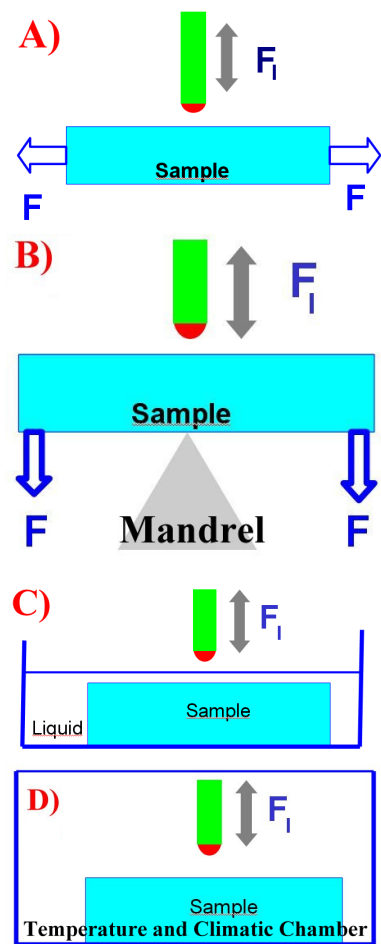


Fig. 4. Contact load testing alternatives, A) multi-axis loading, B) opening a crack, C) loading with the presence of liquid, D) testing under special climatic conditions

Barkhausen noise method will be used. Alternative methods include the measurement of remanent magnetism and residual stress by means of the MMM method (Magnetic Memory of Metals). Measurement of properties and identification of processes taking place during contact loading requires a greater number of tests under a single load and a variable number of cycles. The most common procedure consists in specifying limit conditions for measuring and then performing the measurement. The limits are the number of cycles upon which changes in material begin to take place and the number of cycles leading to such catastrophic destruction that it does not yield any information. There are a number of available testing procedures. Their selection must be based on the service load of the material and on required results.

## 5. Conclusion

The impact tester represents one of the newest and most promising methods for investigation of behaviour of materials subjected to impact contact load. Dynamic loads in the impact tester are concentrated in a small volume of material. This enables examination of behaviour of not only bulk materials but also that of surface films and coatings. The instrument can be expanded with additional measuring equipment, depending on its design. Unique descriptions of behaviour of materials can be obtained using this measuring equipment. No other measuring methods in materials engineering can provide such data. Damping characteristics of materials can be measured using accelerometric measurements. With acoustic emission-based methods, the formation and propagation of impact-induced cracks can be measured based on the amount and frequency of introduced strain energy. The high-frequency impact tester (50 Hz and higher) provides data for plotting Woehler curves. Therefore, the residual life of a part can be assessed using a small sample taken from the part. Another advantage of the high-frequency impact tester is its process of operation, which is closer to the real-world processes involving high frequency impact. A typical example is a cutting process, in which the cutting edge of a tool impacts the work piece surface repeatedly within a short time interval.

The previous chapters contained descriptions of some basic options for testing materials using impact testers and results and conclusions to be derived from the measurements.

## REFERENCES

1. Matthews A., Bantle R.: *Thin Solid Films*, Elsevier, 2004.
2. Bouzakis K.-D., Asimakopoulos A., Michailidis N., Kompoliannis S., Maliaris G., Giannopoulos G., Pavlidou E., Erkens G.: *Thin Solid Films* 469–470, 254 (2004).
3. Kříž A., Beneš P.: *Acta Mechanica Slovaca*, EQUI-LIBRIA, s. 174–180, 2008.

*This paper was prepared with the funding of the MŠMF IM0519 project Research Centre of Rail Vehicles and the internal institutional grant.*

**A. Kříž<sup>a</sup>, P. Beneš<sup>b</sup>, and J. Šimeček<sup>b</sup>** (<sup>a</sup>Department of Material Science and Technology, University of West Bohemia, Faculty of Mechanical Engineering, Czech Republic, <sup>b</sup>Research Centre of Rail Vehicles): **Impact Test of Surface**

This paper deals with selected applications of testing of materials using an impact tester. An impact tester is a piece of testing equipment for investigation of response of materials to repeated impact loads. The principle of the test consists in repeated impacts of a testing body onto the surface of specimen with a specific force. Impact testing is most widely used for testing fatigue properties of those components, which are subjected to repeated impacts and concurrent strong impact shocks. These include machining tools, railway wheels, piston rings and others.

The paper presents results of experiments obtained with an impact tester of authors' own design. It also introduces envisaged development planned for near future: both in terms of design and methodology.

## DYNAMIC NANOINDENTATION OF BOVINE INTERVERTEBRAL END PLATE

**JAROSLAV LUKEŠ\*, JOSEF ŠEPITKA,  
and JIRÍ NEMEČEK**

Czech Technical University in Prague, Faculty of Civil Engineering, Thákurova 7, 16629 Prague 6, Czech Republic  
*jaroslav.lukes@fs.cvut.cz*

---

Keywords: nanoindentation, DMA, viscoelasticity, end plate, intervertebral disc

---

### 1. Introduction

According to recent studies the nanoindentation appears to be a very effective tool to analyze mechanical properties of biomaterials especially in case of hardly accessible soft tissue. Machining of biological material to standardly shaped samples for tensile testing is quite difficult. This paper presents a study of viscoelastic properties of bovine intervertebral disc's end plate (EP) by nanoscale quasistatic and dynamic mechanical analysis (nanoDMA).

Cartilaginous end plate is a part of intervertebral disc that creates the transition zone between hard vertebral body and soft anulus fibrosus (AF). The process of calcification within AF lamellae and EP (Fig. 1) is crucial for mechanical behavior of intervertebral disc. It is observed as the clinical syndrome in childhood and elderly population<sup>1</sup>. Sometimes the etiology is unclear. The previous trauma, surgical intervention or overloading are suggested. Calcification of end plate has critical influence on saline flow to avascular anulus fibrosus end nucleus pulposus and initiates the IVD degeneration<sup>2</sup>. Nanoindentation is an experimental method, which can tell us more about tissue mechanics of end plate<sup>3</sup>.

### 2. Methods

#### 2.1. Sample preparation

Sagittally halved bovine spine was obtained from the butchery. The lumbar spine motion segments were immediately dissected and five millimeter thick plates of vertebral body, end plate and anulus fibrosus were cut and polished under running water condition. Samples were placed into the physiological solution right after. The plate of the sample was glued to the bottom of the Petri dish and surrounded by physiological solution again. The surface was water free and ready to be indented.

#### 2.2. Testing conditions

Quasistatic and nanoDMA load controlled experiments were performed on Hysitron TriboLab® system with the Berkovich diamond tip at the temperature 22.3 °C. Quasistatic loading consisted of three segments 1×50×10 seconds with maximum force  $P_{\max} = 800 \mu\text{N}$  that corresponded to the contact indentation depths  $h_c = 497.66 \pm 74.09 \text{ nm}$ . The time of loading segment  $\tau_L = 1 \text{ s}$  and default sampling frequency 0.017 s provided enough datapoints for the loading curve evaluation. Moreover, it simulated the Heaviside step load function needed for measuring of the pure creep material response. Holding time  $\tau_H = 50 \text{ s}$  corresponded to our previous experience for maximum dwell period of creep data acquisition which is not influenced by the thermal drift error<sup>4</sup>. Unloading segment  $\tau_U = 10 \text{ s}$  was set according to the condition of “fast unloading” described in Vandamme & Ulm<sup>5</sup>.

The same static load was applied to the tip during nanoDMA experiments. Harmonic loading with dynamic load amplitude 20  $\mu\text{N}$  was prescribed for the harmonic frequency range 5–300 Hz. Stiffness  $K_i$  and damping  $C_i$  of the sensor was measured by running a frequency sweep in the air, which is controlled by the software of the Hysitron's system. The procedure was adopted from Asif et al.<sup>6</sup> as well as the analysis of dynamic data.

### 3. Theory

#### 3.1. NanoDMA

Dynamic driving force  $P_0 \sin(\omega t)$  with amplitude  $P_0$  and frequency  $f = \omega/2\pi$  is superimposed on quasistatic loading  $P_{\max}$  and stands for particular term in an equation of motion of the indenter relative to the indenter head:

$$P_0 \sin(\omega t) = m\ddot{x} + C\dot{x} + Kx \quad (1)$$

The solution to the above equation, where compliance  $C = C_i + C_s$  and stiffness  $K = K_i + K_s$  of the system on Fig. 2 are defined respectively, is a steady-state displacement oscillation at the same frequency as the harmonic loading

$$x = X_0 \sin(\omega t - \phi) \quad (2)$$

where  $X_0$  is the amplitude of the displacement oscillation and  $\Phi$  is the phase shift of the displacement with respect to the driving force. Both terms in Eq. (2) are recorded by the nanoindentation system.

The standard analytical solution for the model on Fig. 2, that assumes that the machine frame stiffness  $K_m$  is infinite, follows.

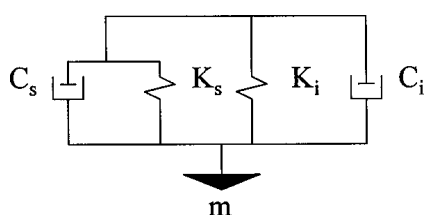


**Fig. 2. Dynamic model of indenter system in contact with the specimen, where  $m$  is the indenter mass,  $C_i$  is the damping coefficient of the air gap in the capacitive displacement sensor,  $C_s$  is the damping coefficient of the specimen,  $K_s$  is the contact stiffness, and  $K_i$  is the spring constant of the leaf springs that hold the indenter shaft. Adopted from Asif et al.<sup>6</sup>**

The amplitude of the displacement signal is

$$X_0 = \frac{P_0}{\sqrt{(K_s + K_i - m\omega^2)^2 + [(C_i + C_s)\omega]^2}} \quad (3)$$

and the phase shift between force and displacement is

$$\varphi = \tan^{-1} \frac{(C_i + C_s)\omega}{K_s + K_i - m\omega^2} \quad (4)$$

where  $m$  is the indenter mass,  $\omega$  is the frequency in rad/s,  $C_i$  is the damping coefficient of the air gap in the capacitive displacement sensor,  $C_s$  is the damping coefficient of the specimen,  $K_i$  is the spring constant of the leaf springs that hold the indenter shaft and  $K_s$  is the contact stiffness<sup>6</sup>.

These calculated values for stiffness and damping of the sample are then used to determine the viscoelastic properties of reduced storage modulus ( $E_r'$ ), loss modulus ( $E_r''$ ) and  $\tan \delta = E_r'/E_r''$  as

$$E_r' = \frac{K_s \sqrt{\pi}}{2\sqrt{A_c}} \quad (5)$$

$$E_r'' = \frac{\omega C_s \sqrt{\pi}}{2\sqrt{A_c}} \quad (6)$$

and

$$\tan \delta = \frac{C_s \omega}{K_s} \quad (7)$$

where  $A_c$  is the contact area based on tip area function related to the contact depth at quasistatic loading<sup>7</sup>. The storage and loss modulus of the sample  $E_s'$  and  $E_s''$ , re-

spectively, are related to the reduced storage and loss moduli by

$$\frac{1}{E_r'} = \frac{(1-v_i^2)}{E_i} + \frac{(1-v_s^2)}{E_s'} \quad (8)$$

$$\frac{1}{E_r''} = \frac{(1-v_i^2)}{E_i} + \frac{(1-v_s^2)}{E_s''} \quad (9)$$

where subscripts  $i$  and  $s$  refer to the indenter and sample materials, respectively, and  $v$  is the Poisson's ratio<sup>8</sup>.

The storage modulus and the loss modulus are related to the complex modulus  $E_s^* = E_s' + iE_s''$  and indicate the ability of the sample to store and return energy (recoverable deformation;  $E_s'$ ) and dissipate energy ( $E_s''$ ). The ratio of the loss modulus to the storage modulus (i.e.,  $\tan \delta$ ) reflects the viscoelastic behavior of the material. It is a material parameter independent of the tip-sample contact area.

### 3.2. Linear Viscoelastic Analysis

In this study, we employed Vandamme and Ulm's isotropic linear viscoelastic model for the nanoindentation creep data analysis<sup>3–5</sup> that adopts two assumptions: (i) material is linearly viscoelastic and (ii) viscous deformation (creep) is associated only with deviatoric deformations. Viscoelastic parameters can be obtained directly from the history of indenter displacement measured during the dwell period at which the load is kept constant. The model utilizes the functional formulation:

$$\varepsilon(t) = \int_0^t C(t-\tau) : \frac{d}{dt} \sigma(\tau) d\tau \quad (10)$$

where  $t$  is time;  $\varepsilon$  is deviatoric strain tensor;  $\sigma$  is deviatoric stress tensor and  $C(t)$  is fourth order tensor of creep functions of the material. The deviatoric compliance function of the 1-D linear viscoelastic Kelvin-Voigt-Maxwell model can be derived in the form:

$$C^d = \frac{1}{G_0} + \frac{1}{G_V} \left( 1 - e^{-\frac{-G_V t}{\eta_V}} \right) + \frac{1}{\eta_M} \quad (11)$$

in which  $G_0$  is the shear modulus,  $\eta_M$  stands for viscosity in Maxwell series unit and  $G_V$ ,  $\eta_V$  are shear modulus and viscosity in the parallel Voigt unit, respectively. The volumetric behavior was considered as purely elastic. Elastic modulus  $E_0$  and associated shear modulus  $G_0 = E_0/2(1-v_0)$  were estimated by the software implemented standard Oliver and Pharr method<sup>7</sup>. Poisson's ratio  $v_0$  was supposed to be time independent for the given material. By the analogy with classical functional formulation of linear visco-

**Table I**  
Material parameters from three fits of indentation creep data

Indent No.	$E_r$ [GPa]	$E_0$ [GPa]	$G_0$ [GPa]	$\eta_v$ [GPa.s]	$\eta_M$ [GPa.s]	$G_v$ [GPa]
1	3.580279	3.223733	1.221111	137.2005	0.2373	0.544
2	3.871679	3.487004	1.320835	151.0563	0.2296	0.5991
3	4.890535	4.408564	1.669911	194.5456	0.6515	1.1106
Avg.	4.114164	3.706434	1.403952	160.934133	0.3728	0.751233
St. dev.	± 0.688	± 0.622	± 0.236	± 29.922	± 0.241	± 0.312

lasticity (Eq. (10)) Vandamme and Ulm identify the fundamental step load solution  $Y(t)$  as the indentation creep function<sup>5</sup>:

$$y(t) = \frac{1}{P_{\max}} \int_0^t Y(t-\tau) \frac{d}{dt} P(\tau) d\tau \quad (12)$$

Once  $Y(t)$  is known, the dimensionless indentation response  $y(t)$  can be determined for any monotonically increasing load history it means loading  $y_L(t)$  and holding  $y_H(t)$  segment of indentation curve. Fitting the creep nanoindentation data by Vandamme and Ulm solution  $y_H(t)$  the viscoelastic parameters are determined as

$$h(t) = \sqrt{\frac{\pi P_{\max} y(t)}{2 M_0 4 \tan \theta}} \quad (13)$$

where  $M_0$  is the instantaneous indentation modulus and  $\theta$  is the half-apex angle of conical indenter. In case of the Berkovich tip the angle  $\theta=70.32^\circ$  (ref.<sup>5</sup>).

#### 4. Results

Shear modulus  $G_0$  is the first input parameter of Vandamme and Ulm's<sup>5</sup> five parameters viscoelastic model (including Poisson's ratio). The fit of nanoindentation creep data (Fig. 3) derives the next three viscoelastic material constants  $\eta_M$ ,  $\eta_v$ ,  $G_v$  (Tab. I). Storage and loss moduli are the characteristics that describe the viscoelastic properties of EP as well. Storage moduli indicate the dependence on frequency as was reported for polymers<sup>8</sup> and articular cartilage<sup>9</sup>, respectively. The values have the increasing trend with the increasing frequency. On the other hand the loss modulus shows almost no dependence on frequency (Fig. 4). The values of storage moduli at low frequencies correspond to elastic reduced moduli from quasistatic indentation  $E_r = 4.11 \pm 0.69$  GPa quite well.

#### 5. Discussion and conclusions

The nanoDMA testing was found to be straightforward method for the identification of viscoelastic parameters of hardly accessible intervertebral cartilaginous end plate. Nanoindentation technique allows biological samples to be surrounded by a physiological solution which prevents a long term degradation of the sample by drying. The experimental set up is very simple in the contrary to standard tensile or compression testing.

Fulcher et al.<sup>9</sup> reported the characteristic limit frequency which was exhibited as a plateau of  $E'$  values at the range to 92 Hz. Such behavior is characteristic for polymer materials where so called glass transition occurs. In case of the cartilage, the plateau could be associated with development of microcracks in the tissue as proposed by Fulcher. However, we did not observe any plateau in storage moduli values over the full range of frequencies 5–300 Hz (Fig. 4). Actually according to this study, the end plate tissue is able to store more energy with higher load rate without the occurrence of inner failures. Further structural studies of EP must be employed in explanation of this end plate behavior.

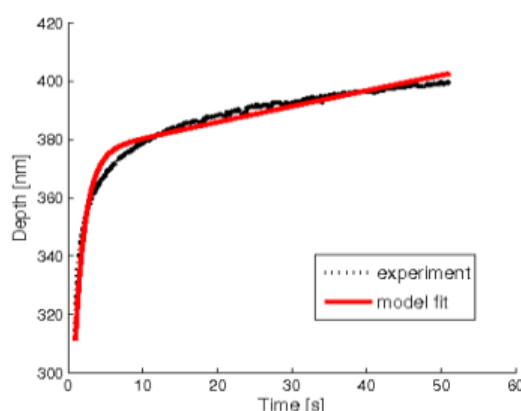


Fig. 3. Nanoindentation creep data fit

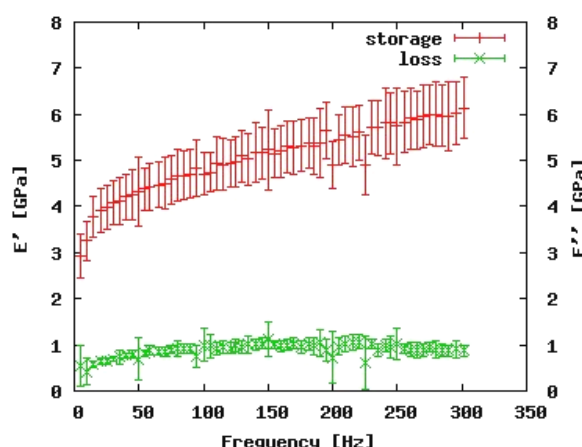


Fig. 4. Storage and loss moduli from nanoDMA

Increasing frequency is connected with the rising load rate.  $E'$  clearly showed this dependence which is another proof of a viscoelastic manner of the material.

The Maxwell-Kelvin-Voight model's viscoelastic parameters complement the information about the material of the end plate. The material behavior during the dwell period clearly confirmed the viscoelastic behavior of the EP as well. Especially, the viscosity of the Maxwell unit was quite significant.

Generally, the material properties of biological tissues change from region to region. This is due to the microstructural heterogeneities and varying architecture. Mapping of mechanical properties at different region was left as a future task. This study shows novel approach and potential utilization of nanoindentation technique for biomechanics and tissue mechanics, respectively.

*Supports of the Ministry of Industry and Trade of Czech Republic MPO CZ, FT-TA3/131 and Ministry of Education of the Czech Republic MSM 6840770003 are gratefully acknowledged.*

## REFERENCES

- Chanchairujira, K., Chung, C. B., Kim, J. Y., Papakonstantinou, O., Lee, M. H., Clopton, P., Resnick, D.: Radiology 230, 499 (2004).
- Peng, B., Hou, S., Shi, Q., Jia, L.: Chinese Medical J. 114, 308 (2001).
- Lukes, J., Mares, T., Nemecek, J., Otahal, S.: IFMBE Proceedings 23, 1792 (2009).
- Lukes J., Nemecek J., Minster J.: 25<sup>th</sup> Danubia-Adria Symposium on Experimental Methods in Solid Mechanics, 161–162 (2008).
- Vandamme M., Ulm F.-J.: Int. J. Solids Structures 43, 3142 (2006).
- Asif S. A. S., Wahl K. J., Colton R. J.: Rev. Sci. Instrum. 70, 2408 (1999).
- Oliver W. C., Pharr G. M.: J. Mater. Res. 7, 1564 (1992).
- Chakravartula A., Komvopoulos K.: Appl. Phys. Lett. 88, 131901 (2006)
- Fulcher G. R., Hukins D. W. L., Shepherd D. E. T.: BMC Musculoskeletal Disorders 10, 61 (2009).

**J. Lukeš<sup>a</sup>, J. Šepitka<sup>a</sup>, and J. Němcék<sup>b</sup>** (<sup>a</sup>Czech Technical University in Prague, Faculty of Mechanical Engineering, <sup>b</sup>Czech Technical University in Prague, Faculty of Civil Engineering): **Dynamic Nanoindentation of Bovine Intervertebral End Plate**

According to recent studies nanoindentation appears to be a very efficient tool to analyze mechanical properties of biomaterials especially in case of hardly accessible soft tissue. This paper presents a study of viscoelastic properties of bovine intervertebral disc's end plate (EP) by nanoscale quasistatic and dynamic mechanical analysis (nanoDMA). The sample was kept in physiological conditions although the surface was water free. The effect of frequency on storage modulus  $E'$ , loss modulus  $E''$  and a comparison with simple linear viscoelastic solution fitted from the dwell period in quasistatic loading have been shown and discussed in this paper in some details.

## CHANGES OF MICROMECHANICAL PROPERTIES OF ULTRA HIGH MOLECULAR WEIGHT POLYETHYLENE AFTER ELECTRON BEAM IRRADIATION AND UNIAXIAL COMPRESSION

**JOANNA MASZYBROCKA\*, JERZY CYBO, and ADRIAN BARYLSKI**

*University of Silesia, Faculty of Computer Science and Materials Science, Sniezna 2, 41-200 Sosnowiec, Poland  
joanna.maszybrocka@us.edu.pl*

**Keywords:** ultra-high-molecular-weight polyethylene, uniaxial compression, electron beam irradiation, micromechanical properties.

### 1. Introduction

For over 40 years, UHMWPE (Ultra High Molecular Weight Polyethylene) has been a material widely applied in the production of bearing elements of endoprostheses used in total alloplasty of joints. In spite of the numerous undeniable advantages of this material, there are certain factors which reduce the possibility of long-lasting presence of an implant in the human organism. High susceptibility of polyethylene to plastic deformation and abrasive wear is considered one of the most serious problems<sup>1,2</sup>. A key element in selecting and forecasting operational durability of a material and its upper layer is the ability to identify its micromechanical properties. Consideration of the relationship between the properties obtained as a result of modifications and their changes induced by operational factors cannot be neglected, either. These results from the fact that the main effect of the tribological process is undoubtedly associated with local changes of the micromechanical properties, which occur on the friction surface and in the subsurface layer (to 20 µm).

The research conducted by the authors has shown that the friction surface exhibits numerous traces of permanent deformation in the form of crosswise projections, located along the irregularities consistent with the friction direction<sup>2-4</sup>. The size and distance between the projections testify to susceptibility of the polymer to plastic flow (Fig. 1). A simultaneous reorientation of lamellae on the friction surface and in the upper layer is a consequence of permanent deformation induced by friction<sup>2-4</sup>.

Among the contemporary methods of mechanical testing, those performed using the microindentation method play an increasingly important role. Availability of methods of continuous and precise recording of the depth of penetration of an indenter of a known geometry as a function of prescribed load and time enables determining not only hardness and the elastic modulus, but also a number of elastic and plastic properties, thereby ensuring

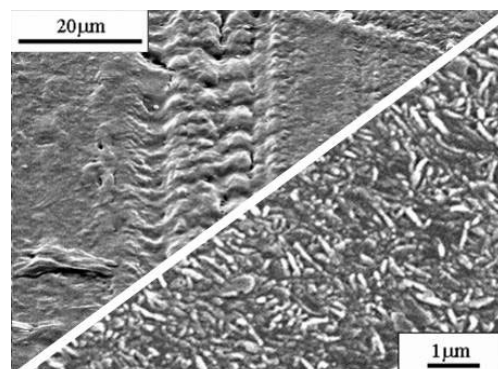


Fig. 1. Plastic deformation of the friction surface of polymer and lamellae orientation in the friction zone

a comprehensive characterisation of micromechanical properties of the material.

This paper aims to evaluate the effectiveness of radiation modification of polyethylene intended for endoprosthetic elements in reducing the consequences of plastic deformation in microregions of the upper layer. The results obtained are an important link in the discussion focused on the description of the phenomena (on different scales) and processes which provide a theoretical basis for effective shaping of polyethylene intended for frictional interaction in the polymer – metal system. The discussion also includes an analysis of the nature and scale of consequences of the tribological process.

### 2. Research Material

The object of the research consisted of the currently produced ultra high molecular weight polyethylene for medical applications, GUR 1050 (Poly Hi Solidur Deutschland GmbH). Irradiation of the material with an electron-beam (of 10 MeV) and with doses of different values (0 kGy, 2 × 26 kGy, 4 × 26 kGy) enabled obtaining variants with a variable degree of cross-linking. The specimens were loaded (compressed) uniaxially, so as to obtain diverse effective plastic deformation ( $e_f$ ) in the polymer material. Total deformation of  $Z_c = 0-80\%$  was applied and various levels of effective plastic deformation were obtained:  $e_f = 0-0.7$  (ref.<sup>5</sup>). The value of effective plastic deformation was calculated as:

$$e_f = \ln \frac{h_0}{h_k} \quad (1)$$

where:  $h_0$  – initial height of the specimen,  $h_k$  – height of the specimen after work hardening (5 days after test).

### 3. Research Methodology

The degree of crystallinity of the polymer variants investigated was determined via differential scanning calorimetry (DSC), using a thermoanalyser of TA Instruments, type DSC 2010. The melting point was determined on a thermogram for the maximum of an endothermic peak of melting. The degree of crystallinity was calculated from the formula:

$$C_{\text{DSC}} = \frac{\Delta H_f}{\Delta H_c} \cdot 100\% \quad (2)$$

where  $\Delta H_f$  – the heat of phase transition (i.e. melting) of the investigated polymer specimen, determined from a DSC thermogram [ $\text{J g}^{-1}$ ];  $\Delta H_c$  – the heat of phase transition of completely crystalline polyethylene (empirically determined value amounting to  $290 \text{ J g}^{-1}$ ).

Measurements of micromechanical properties were performed using Micron-Gamma equipment. A Berkovich indenter with a pyramid angle of  $65^\circ$  was used under the load of 1 N, at a speed of load escalation and unloading rate of  $1 \text{ N min}^{-1}$ , and load time of the specimen under maximum pressure: 15 s.

The hardness was determined as a ratio of the maximum load imposed on the indenter and the projection contact area,  $A_p$ , the latter being a function of the indenter shape at the contact depth,  $h_c$ :

$$H = \frac{P_{\text{max}}}{A_p} \quad (3)$$

where  $P_{\text{max}}$  – maximum load imposed on the indenter,  $A_p$  – projection contact area.

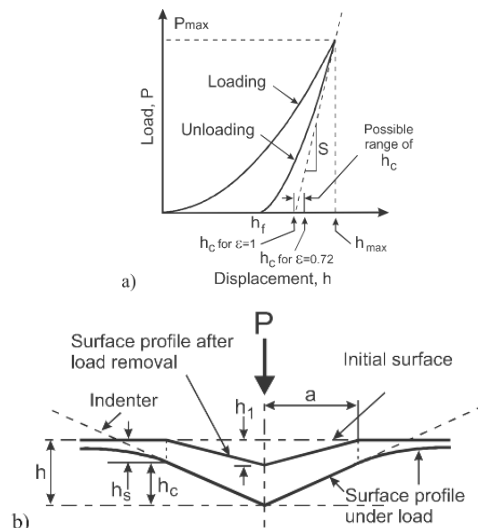


Fig. 2. a) Loading-unloading curve as a function of displacement, b) material deformation during hardness examination

According to the Olivier-Pharr method<sup>6</sup>, the elastic modulus was determined while taking into account the slope of tangent to the initial part of the unloading curve (Fig. 2). The unloading curve is described with an exponential function in the following form:

$$P = \alpha(h - h_f)^m \quad (4)$$

where  $\alpha$  – a constant including the elastic modulus and Poisson's ratio of materials of the specimen and the indenter,  $h_f$  – the depth of indentation after unloading, m – an exponent depending on the indenter geometry.

By differentiating the equation (4) with respect to the penetration depth  $h$  and calculating the value for  $h = h_{\text{max}}$ , the slope of the initial portion of the unloading curve ( $S$ ) was determined:

$$S = \left( \frac{dP}{dh} \right)_{h=h_{\text{max}}} \quad (5)$$

$$S = \alpha m (h_{\text{max}} - h_f)^{m-1} \quad (6)$$

On this basis, the contact depth,  $h_c$ , was determined:

$$h_c = h - \varepsilon \frac{P_{\text{max}}}{S} \quad (7)$$

where  $\varepsilon$  – constant dependent on the indenter geometry.

The formulas quoted above allowed determining a reduced elastic modulus of,  $E_r$ , from the dependence:

$$E_r = \frac{\sqrt{\pi} \cdot S}{2 \cdot \beta \cdot \sqrt{A_p(h_c)}} \quad (8)$$

where  $S$  – contact stiffness,  $A_p$  – contact area, with taking account of permanent deformation,  $\beta$  – correction constant for the indenter tip shape (for Berkovich indenter,  $\beta \approx 1,034$ ).

The reduced modulus,  $E_r$ , is used to account for the fact that elastic displacements occur in both the indenter and the sample. The elastic modulus of the test material,  $E$ , is calculated from  $E_r$ , using:

$$\frac{1}{E_r} = \frac{1 - v^2}{E} + \frac{1 - v_i^2}{E_i} \quad (9)$$

where  $E$ ,  $v$  – elastic modulus and Poisson's ratio for the investigated material,  $E_i$ ,  $v_i$  – elastic modulus and Poisson's ratio for the material of the indenter (for diamond  $E = 1141 \text{ GPa}$ ,  $v = 0.07$ ).

The loading-unloading curve was the source of information on the trend of material deformation during the test (Fig. 3 a–c) and enabled determining the following

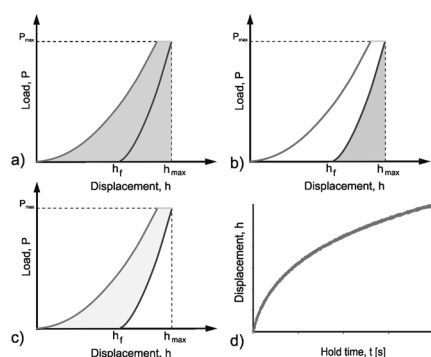


**Fig. 3. Analysis of the loading-unloading curve:** a) The total work of indentation, b) elastic work of deformation, c) plastic work of deformation, d) creep during the indentation test

parameters:  $W_{\text{tot}}$  – the total work of indentation (the entire area under the recorded loading curve),  $W_{\text{sp}}$  – elastic work of deformation (the area under the unloading curve),  $W_{\text{pl}}$  – plastic work of deformation (the area between the loading and unloading curves).

During the indentation test, UHMWPE specimens were exposed to the maximum load at  $t = 15$  s, and, at the same time, an evaluation of susceptibility of the individual material variants to flow,  $\Delta h$ , was made (Fig. 3d).

## 4. Results and Discussion

The changes in the structure and properties of polyethylene induced by radiation modification have a significant impact on the behaviour of the material un-

der load during service.

When analysing the specimens that were not subjected to radiation modification (input polymer BZ), it has been found that compressive stresses and the resultant UHMWPE work hardening induced a reduction of hardness,  $H$ , and elastic modulus,  $E$ , proportional to plastic deformation,  $e_f$  (Fig. 4e–f). An increasing degree of work hardening also results in higher susceptibility of the material to creep, as well as to plastic,  $W_{\text{pl}}$ , and elastic deformation,  $W_{\text{sp}}$  (Fig. 4a–d). The electron beam irradiation results in increased hardness and elastic modulus of the polyethylene variants tested (Fig. 4e–f), which depends on the dose applied ( $2 \times$ ,  $4 \times$ ). Moreover, susceptibility to creep becomes reduced as well, which is manifested through decreased increment of the depth of penetration under load,  $\Delta h$  (Fig. 4d). An increased irradiation dose provokes a decreased value of the work of indentation,  $W_{\text{tot}}$ , and its components,  $W_{\text{sp}}$  and  $W_{\text{pl}}$ , (Fig. 4a–c) and an increase of the energy necessary to create a permanent indentation of unit volume, thereby indicating reduced susceptibility of the polymer to deformation during exposure to service load.

In view of the fact that examinations of the polymer morphology are pending, the attempt to explain the observed trends in changes of the micromechanical properties was based on an analysis of the degree of crystallinity (Fig. 5). A convergence was found between the changes of the degree of crystallinity and the trend of changes of the micromechanical properties ( $H$ ,  $E$ ).

Irradiation of the material with an electron beam results in an increased degree of crystallinity, which depends on the dose applied. In both, the initial material and the electron-irradiated material, the degree of crystallinity decreases as the plastic deformation grows, which means

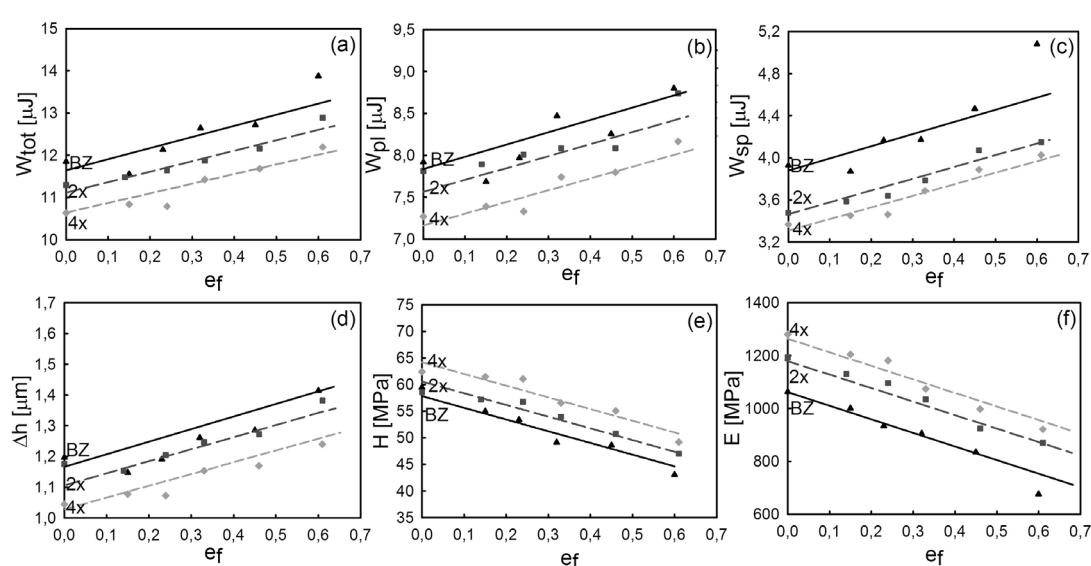


**Fig. 4. Micromechanical characteristics of the samples GUR 1050**

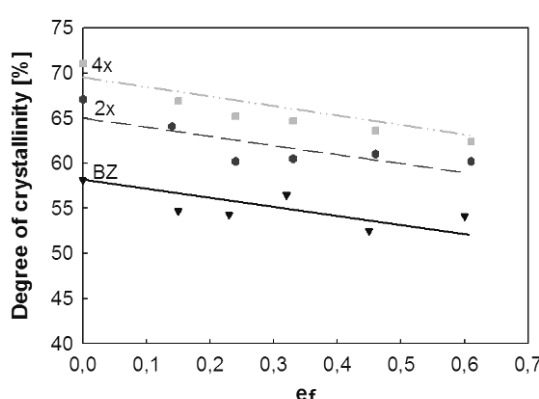


Fig. 5. A change of the degree of crystallinity of the specimens

that modification through radiation does not prevent the particular variants from a decrease in the degree of crystallinity in the whole range of deformation.

## 5. Conclusions

It is shown in the paper that an evaluation of micro-mechanical properties by means of microindentation is a significant link in the evaluation of the effectiveness of factors shaping the structure and properties of polyethylene, including, in particular, microregions in the upper layer, and of the influence of operational factors on their change. It is extremely important for reasons regarding the application of this polymer. An insignificant change of its local micromechanical properties may result in increased wear and occurrence of undesirable wear products (such as submicron particles) which, in consequence, lead to osteolysis<sup>7</sup>. The method applied responds very sensitively to both the irradiation conditions (total radiation dose) and the deformation degree of the specimen. It has been shown that cross-linking of polyethylene as a result of electron irradiation of the input polymer GUR 1050 ensures: a reduction of creep, decreased susceptibility to absorbing the deformation work, enhanced resistance to permanent deforma-

tion and increased hardness and elastic modulus in the whole range of work-hardening. The determined local micromechanical characterization of polyethylene will, in the subsequent research phase, be supplemented with morphological and macro tests carried out on tribological testers.

## REFERENCES

- Kurtz S., in book: *The UHMWPE Handbook: Ultra-High Molecular Weight Polyethylene in Total Joint Replacement*. Elsevier Academic Press, San Diego 2004.
- Maszybrocka J., in PhD thesis: *Micromechanical properties and effects of operation in friction couple of polyethylene formed by means of initial deformation and irradiation with electrons.*, University of Silesia, Katowice 2005.
- Maszybrocka J., Cybo J., Frąckowiak J.: Mater. Sci. Forum 513, 75 (2006).
- Maszybrocka J., Cybo J., Cwajna J.: Mater. Characterization 60, 1139 (2009).
- Barylski A., Cybo J., Maszybrocka J.: Czasopismo Techniczne 3, n3 (2009).
- Oliver W. C., Pharr G. M.: J. Mater. Res. 7, 1546 (1992)
- Zhu Y. H., Chiu K. Y., Tang W. M.: J. Orthopaedic Surgery 9, 91 (2001).

**J. Maszybrocka, J. Cybo, and A. Barylski** (*University of Silesia, Faculty of Computer Science and Materials Science, Poland*): **Changes of Micromechanical Properties of Ultra High Molecular Weight Polyethylene after Electron Beam Irradiation and Uniaxial Compression**

The microindentation method was applied in the study to determine a complex micromechanical characterization of microregions of the UHMWPE polymer applied for endoprosthesis cups. It has been shown that the methodology applied responds very sensitively to both the irradiation conditions (total radiation dose) and the deformation degree of the specimen, constituting thereby a significant link in the evaluation of the effectiveness of factors shaping the structure and properties of polyethylene and, in particular of microregions of the upper layer.

## EVALUATION OF AU THIN FILM ON POLYETHYLENE AND GLASS

**ROSTISLAV MEDLÍN<sup>a\*</sup>, OLGA BLÁHOVÁ<sup>a</sup>, and VÁCLAV ŠVORČÍK<sup>b</sup>**

<sup>a</sup>New Technologies – Research Centre, University of West Bohemia, Univerzitní 8, 306 14 Plzeň, Czech Republic,

<sup>b</sup>Department of Solid State Engineering, Institute of Chemical Technology, 166 28 Prague, Czech Republic  
medlin@ntc.zcu.cz

Keywords: polyethylene, glass, plasma treatment, Au sputtering, mechanical properties, surface morphology

### 1. Introduction

Metal-polymer composites are suitable for many applications, especially in microelectronics<sup>1</sup>. Mutual interaction between metal and polymers is generally very weak but it can be increased if the polymer surface is modified before metal deposition. Several techniques of modification (physical, chemical or their combination) have been suggested for enhancing the metal adhesion<sup>2,3</sup>.

Gold nanoparticles, due to their unique electrical, optical and photophysical properties, are expected to provide a variety of potential applications for electronics<sup>4–7</sup>. Well known properties such as stability, non-reactivity and bioinertness of gold are used with advantage in medical diagnostics<sup>8</sup>, Raman spectroscopy<sup>9</sup>, biological imaging<sup>10</sup> and biosensors<sup>11</sup>. Gold nanoparticles are promising structures for biomedical applications, structures combining gold nanoparticles with polymers<sup>12–14</sup>.

Since gold is the most inert metal, the adhesion between gold particles and polymers is expected to be very poor. However, gold can easily react with thiol ( $-SH$ ) groups, which can be fixed on the polymer surface modified in a proper manner. The polymer surface can efficiently be modified by irradiation with plasma, ultraviolet light from an excimer lamp or by ion irradiation<sup>15–18</sup>.

Polyethylene (PE) and glass were treated in Ar plasma discharge and then grafted from methanol solution of 1,2-ethanedithiol to enhance the adhesion of gold nanoparticles or sputtered gold layers. The modified PE samples were either immersed into freshly prepared colloid solution of Au nanoparticles or covered with 50 nm thin sputtered gold nanolayer.

In this work, the surface of the substrate was modified by plasma discharge and subsequently grafted with 1,2-ethanedithiol to introduce thiol ( $-SH$ ) groups. Short dithiol is expected to be fixed via one of  $-SH$  groups to radicals created by the preceding plasma treatment. Next, the free –

SH groups are allowed to interact either with gold nanoparticles or with gold atoms from the sputtered Au nanolayer.

The main goal of this study is to examine the effect of the plasma treatment and dithiol grafting on the binding of gold nano-particles and on the adhesion of sputtered gold layer on the substrate.

The surface morphology was study by AFM. The nanoindentation equipment was used to determine micro-hardness and elasticity modulus and to perform nano-scratch tests. SEM was used for documentation of scratchs.

### 2. Experimental Materials

The gold layers were sputtered on  $2 \times 2$  cm microscopic glass (1 mm thick). Surface roughness of glass of  $R_a = 0.34$  nm was measured in an area of  $1.5$  mm $^2$ . The sputtering was accomplished with Balzers SCD 050 device from a gold target (99.99% purity, supplied by Goodfellow Ltd.). Oriented, high-density polyethylene (PE,  $\rho = 0.952$  g cm $^{-3}$ ) in the form of 40  $\mu$ m thin foils (supplied by Granitol Ltd., Czech Republic) was used in the next experiments. The samples were modified in diode plasma discharge with Balzers SCD 050 device for the time of 240 s. DC Ar plasma was obtained under the following conditions: Ar gas purity of 99.997 %, discharge power of 8.6 W.

Four glass samples were modified by plasma for 100 and 400 s, respectively. Two plasma-modified samples were then grafted for 12 h from methanol solution of 1,2-ethanedithiol. In the next experiment both pristine, plasma modified and dithiol grafted glass samples were coated with 50 nm thin sputtered Au layer (see Fig. 1). The sputtering was performed with the same Balzers SCD 050 device.

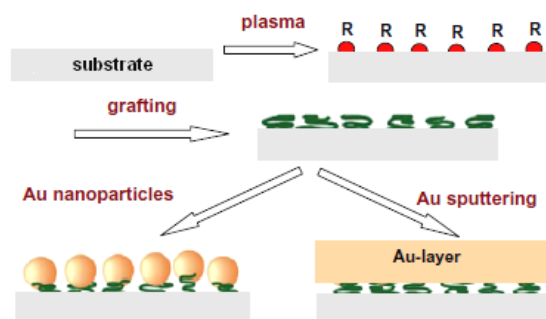


Fig. 1. Scheme of polymer modification with plasma discharge (R-radical), grafting by dithiol and by either coating with Au nanoparticles or sputtering of Au nanolayer<sup>19</sup>

### 3. Experimental Techniques

The thickness of the metal layer for chosen sputtering times was examined using atomic force microscopy (AFM). The AFM images were taken under ambient conditions on a Digital Instruments CP II device. A large area scanner was used, allowing an area up to  $100 \mu\text{m}^2$  to be imaged (see Fig. 2).

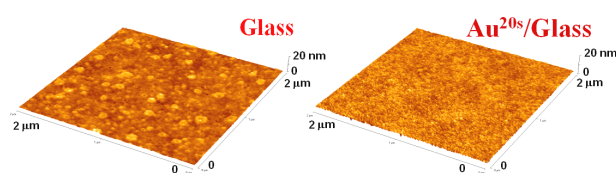


Fig. 2. AFM image of the glass (Glass) and glass 20 s sputtered with Au ( $\text{Au}^{20s}/\text{Glass}$ )

Nanoindentation and nanoscratches were carried out by Nano Indenter XP with CSM module (Fig. 3). This additional device allows recording of the contact stiffness during the whole process of indentation. The principle of this measurement is oscillation along the primary load direction with the frequency from 0.05 to 200 Hz and amplitude from 60 to 300 mN. The instrument analyses the dynamic response of the tested material and according to the response, the device can estimate material parameters like hardness and modulus of elasticity.

The contact depth  $h_c$  was determined as follows:

$$h_c = h - \varepsilon \frac{P_{\max}}{S} \quad (1)$$

where  $h$  is the total indenter displacement corresponding to the load  $P_{\max}$ ,  $\varepsilon$  is a correction factor for the non-circular shapes of the indenter (for Berkovich indenter  $\varepsilon = 0.75$ ), and  $S$  is the contact stiffness. The reduced elastic modulus  $E_r$  was determined from the dependence:

$$E_r = \frac{\sqrt{\pi} \cdot S}{2 \cdot \beta \cdot \sqrt{A_p(h_c)}} \quad (2)$$

where  $S$  is contact stiffness,  $A_p$  is contact area, taking account of permanent deformation,  $\beta$  is correction constant for the indenter shape (for Berkovich indenter  $\beta \approx 1.034$ ). The reduced modulus  $E_r$  is used to account for the fact that elastic displacements occur in both the indenter and the sample. The elastic modulus of the test material  $E$  is calculated from  $E_r$  using:

$$\frac{1}{E_r} = \frac{1 - v^2}{E} + \frac{1 - v_i^2}{E_i} \quad (3)$$

where  $E$ ,  $v$  is elastic modulus and Poisson's ratio for the investigated material,  $E_i$ ,  $v_i$  is elastic modulus and Pois-

son's ratio for the material of the indenter (for diamond  $E = 1141 \text{ GPa}$ ,  $v = 0.07$ ).

The hardness was determined as a ratio of the maximum load  $P_{\max}$  imposed on the indenter and the projection contact area  $A_p$  with a function of the indenter shape at the contact depth ( $h_c$ ):

$$H = \frac{P_{\max}}{A_p(h_c)} \quad (4)$$



Fig. 3. Nanoindenter XP and SEM Quanta 200

### 4. Results and discussion

Figs. 4 and 5 show the measured curves representing the dependency of indentation hardness and modulus of elasticity on the indentation depth. For grafted polymer (modified in plasma 100 and 400 s – ST1 and ST4), it is apparent that both hardness and modulus of elasticity have slightly increased. Changes in SP1 and SP4 (glass treated 100 and 400 s) were negligible when compared with the S specimen (pristine glass with Au layer).

Created scratches were documented using SEM Quanta 200. In the process of creation of this scratch the tip was gradually loaded from 0 to 20 mN. Fig. 6 shows tracks of the indenter in the 50 nm thick Au film deposited on pristine PE (A – PE/Au), plasma treated PE (B – PE/plasma/Au) and plasma treated and dithiol grafted PE (C – PE/plasma/SH/Au). Measurement showed that grafting of the plasma activated PE surface with dithiol significantly increases the adhesion of sputtered Au nanolayer on modified polymer (see<sup>19</sup>).

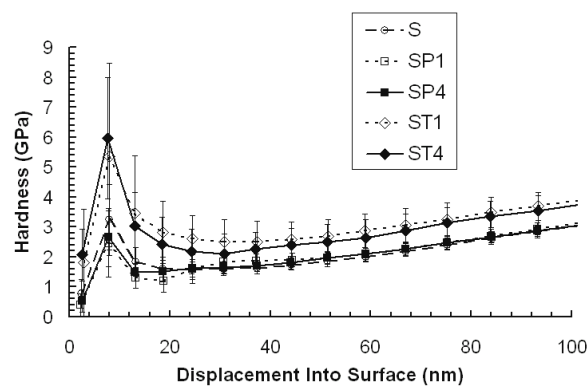


Fig. 4. Dependence of indentation hardness on the indentation depth

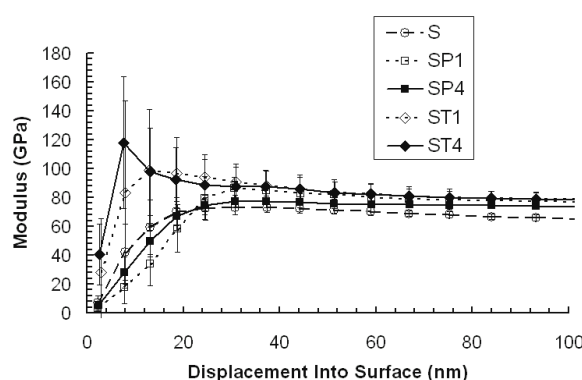


Fig. 5. Dependence of indentation modulus hardness on the indentation depth

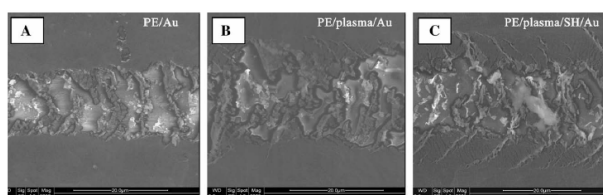


Fig. 6. SEM images of the scratch path on the Au layer on (A) pristine PE, (B) plasma treated PE and (C) plasma treated and dithiol grafted PE<sup>19</sup>

The scratches were measured for evaluation in the place where the indenter reached the substrate.

Fig. 7 shows scratches in ST1 and ST4 specimens. Fig. 8 shows the initial part of scratch of the Au film. Initial sections of scratches have been documented in order to determine the critical load: photographs were used for measurement of the distance, at which the indenter penetrated the film and reached the substrate (see Fig. 9).

All scratches have been documented by means of SEM and the locations where substrate was revealed have been identified. Known loading rate and travel speed of the specimen were used to determine the critical load  $L_c$ , needed for the indenter to penetrate the film and reach the substrate.

The values of the critical load  $L_c$  for penetration of the Au layer and reaching substrate are in Table I.

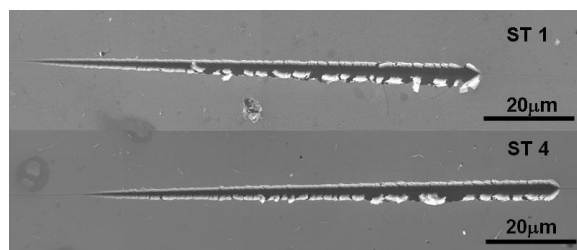


Fig. 7. SEM image of the scratch – composed of multiple snapshots

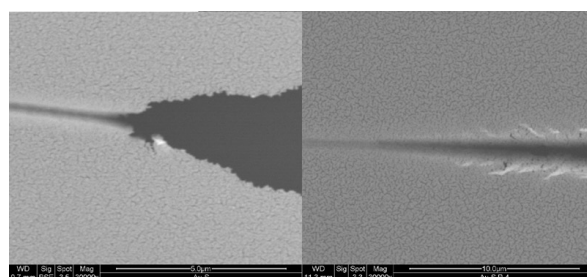


Fig. 8. SEM image of the initial part of scratch path on glass (S-left) and plasma treated glass (SP4-right)

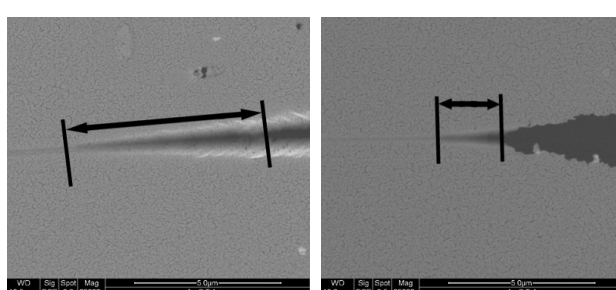


Fig. 9. Measure of critical loads from SEM images on ST1 (left) and ST4 (right)

Table I  
Critical load for measured samples

Sample	S	ST1	ST4	SP1	SP4
$L_c$ [mN]	0.11	0.68	0.44	0.12	0.44

## 5. Conclusions

Specimens with the Au film on glass were tested by nanoindentation, which yielded the values of indentation hardness and indentation modulus of elasticity. In addition, a nanoscratch test has been carried out.

Results show that the critical loads for Au layers were very small, but depended on substrate preparation. For glass modified only 100 s (ST1),  $L_c$  is higher than for glass treated 400 s (ST4 and SP4).

Furthermore, it was found that the sole plasma treatment does not affect local mechanical properties, in contrast to specimens, which underwent the grafting process and exhibited a slight increase in hardness and modulus of elasticity. Nanoscratch measurement showed that the grafting of plasma activated glass surface with dithiol increases significantly the adhesion of sputtered Au nanolayer to glass.

The work has been supported by the GACR under projects 106/09/0125 and 108/10/1106.

## REFERENCES

1. Li Z., Friedrich A., Taubert A.: *J. Mater. Chem.* **18**, 1008 (2008).
2. Švorčík V., Kotál V., Slepčka P., Bláhová O., Šutta P.: *Polym. Eng. Sci.* **46**, 1326 (2006).
3. Kotál V., Švorčík V., Slepčka P., Bláhová O., Šutta P., Hnatowicz V.: *Plasma Proc. Polym.* **4**, 69 (2007).
4. Haruta M.: *Gold Bull* **37**, 27 (2004).
5. Tahara M., Cuong N. K., Nakashima Y.: *Surf. Coat. Tech.* **174**, 826 (2003).
6. Daniel M. C., Astruc D.: *Chem. Rev.* **104**, 293 (2004).
7. Goia D. V.: *J. Mater. Chem.* **14**, 451 (2004).
8. Cheng M. M. C., Cuda G., Bunimovich Y. L., Heath J. R., Mirkin C. A., Nijdam A. J., Terracciano R., Thundat T., Ferrari M.: *Curr. Opin. Chem. Biol.* **10**, 11 (2006).
9. Hering K., Cialla D., Ackermann K., Dorfer T., Moller R., Mattheis R., Fritzsche W., Rosch P., Popp J.: *Anal. Bioanal. Chem.* **390**, 113 (2008).
10. Hainfeld J. F., Slatkin D. N., Smilowitz H. M.: *Phys. Med. Biol.* **49**, 309 (2004).
11. Sinha A. K., Seelan S., Tsubota S., Haruta M.: *Top. Catal.* **29**, 95 (2004).
12. Taubert A., Wiesner U. M., Muellen K.: *J. Mater. Chem.* **13**, 1090 (2003).
13. Tseng R. J., Huang J. X., Ouyang J.: *Nano Lett.* **5**, 1077 (2005).
14. Ishida T., Kuroda K., Minagawa W., Haruta M.: *J. Colloid Interf. Sci.* **323**, 105 (2008).
15. Bačáková L., Walachová K., Švorčík V., Hnatowicz V.: *J. Biomater. Sci. Polym.* **12**, 817 (2001).
16. Heitz J., Švorčík V., Bačáková L., Ročková K., Ratajová E., Gumpenberger T., Bauerle D., Dvořáková B., Kahr H., Graz I., Romanin C.: *J. Biomed. Mater. Res.* **67A**, 130 (2003).
17. Slepčka P., Kolská Z., Náhlík J., Hnatowicz V., Švorčík V.: *Surf. Interf. Anal.* **41**, 741 (2009).
18. Siegel J., Slepčka P., Heitz J., Kolská Z., Sajdl P., Švorčík V.: *Appl. Surf. Sci.* **256**, 2205 (2010).
19. Švorčík V., Chaloupka A., Záruba K., Král V., Bláhová O., Macková A., Hnatowicz V.: *Nucl. Instr. Meth. B* **267**, 248 (2009).

**R. Medlín<sup>a</sup>, O. Bláhová<sup>a</sup>, V. Švorčík<sup>b</sup>** (<sup>a</sup>New Technologies – Research Centre, University of West Bohemia, Plzeň, <sup>b</sup>Department of Solid State Engineering, Institute of Chemical Technology, 166 28 Prague, Czech Republic): **Evaluation of Au Thin Film on Polyethylene and Glass**

Polyethylene and glass were treated in Ar plasma discharge and then grafted from methanol solution of 1,2-ethanedithiol to enhance the adhesion of gold nanoparticles or sputtered gold layers. Properties of the plasma modified, dithiol grafted and gold coated glass were studied using nanoindentation and SEM. Nanoindentation was used to determine microhardness and elasticity modulus and to perform scratch tests. Nanoscratch measurement showed that the grafting of plasma activated glass surface with dithiol increases significantly the adhesion of sputtered Au nanolayer to glass.

## THE HARDNESS ANALYSIS OF THE IF STEEL SHEET AFTER A PLASTIC DEFORMATION

**MÁRIA MIHALIKOVÁ\*, ĽUBOMÍR AMBRIŠKO, and LADISLAV PEŠEK**

*Department of Materials Science, Faculty of Metallurgy,  
Technical University of Košice, Letná 9, 042 00 Košice,  
Slovak Republic  
maria.mihalikova@tuke.sk*

Keywords: plastic deformation, automotive steel sheet, hardness

### 1. Introduction

Automotive steels can be classified in several different ways. One is by a metallurgical designation. Common designations include low-strength steels (interstitial-free and mild steels); conventional HSS (carbon-manganese, bake hardenable, high-strength interstitial-free, high-strength, low-alloy steels); and the newer types of AHSS (dual phase, transformation-induced plasticity, complex phase, and martensitic steels). Additional higher strength steels for the automotive market include ferritic-bainitic, twinning-induced plasticity, nano, hot-formed, and post-forming heat-treated steels<sup>1,2</sup>. Another classification method important to part designers is strength of the steel. One such system defines High-Strength Steels (HSS) with yield point  $R_y$  from 210 to 550 MPa and tensile strength  $R_m$  in the range 270–700 MPa, while Ultra-High-Strength Steels (UHSS) steels have yield strength higher than 550 MPa and tensile strength higher than 700 MPa. These arbitrary ranges suggest discontinuous changes, when moving from one category to another. The steel characteristics drafted as was mentioned enable, that the automobile designer can realize their imaginings to reduce of a construct weight and to increase crew safety personnel on a craft accident<sup>1–3</sup>.

Behavior of IF steel has been observed in this contribution. Steels were loaded by static tension by the loading rate  $1.3 \text{ mm min}^{-1}$ . Videoextensometry method has been used for scanning of the distribution of deformation just before fracture. Several experimental techniques exist for non contact deformation measuring.

Experimental equipment consists of CCD (Charge Coupled Device) camera and computer, which serves for the process of the camera signal by corresponding software. Suitable contrast marks (dots) are dashed on the scanned surface of the specimen and after the specimen is illuminated during the measurement by diffuse light in such manner to obtain the best contrast between the specimen surface and dashed dots. PC program records co-

ordinates of the gravity centre of individual dots during test and also enables to save a picture sequences synchronously<sup>4,5</sup>.

### 2. Experimental material and methods

Specimens from IF (interstitial free) cold rolled steel sheets with thickness of 1.8 mm were used for tensile tests. Mechanical properties are specified in Tab. I and chemical compositions in Tab. II. Specimens were taken transversal to the rolling direction.

Microstructure of steels (Fig. 1) was observed by light microscope OLYMPUS.

Table I  
Mechanical properties

Steel	Mechanical properties		
	$R_{p0.2}$ [MPa]	$R_m$ [MPa]	$A_5$ [%]
IF	185	300	45

Table II  
Chemical compositions

Steel	C	S	Mn	Al	Nb	V	Ti
IF	0.001	0.010	0.082	0.055	0.001	0.002	0.040

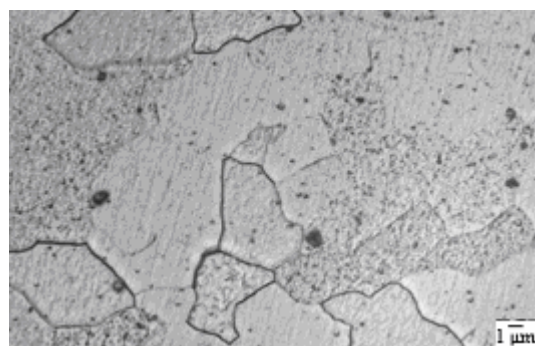


Fig. 1. Microstructure of the IF steel

Due to absence of interstices the IF steels have low yield point and high ductility. These steels are immune towards ageing process and they are suitable for large shapes complicated car body pressworks. IF steel is used mainly for extremely deep drawing. High plasticity is available by reducing of carbon contents less than

$C < 0.005\%$  and by micro-alloyed process with Ti, Nb, or combination Ti + Nb, which completely bind interstices elements C, N on a stable precipitates (Fig. 1).

Tensile test was performed on a plane specimens. The width of specimen was reduced from both sides approx. 1 mm in the centre on a length of 20 mm. The reduction caused that fracture will occur just in this area. Record of the test was made by CCD camera with a resolution of  $640 \times 480$  pixels. A scanning area of specimen was covered with a grid of  $9 \times 22$  dots with 1.0 mm step. Surface of specimen was scanned during whole tensile test by CCD camera and longitudinal deformations  $\varepsilon_y$  (parallel with the direction of loading) and transverse deformations  $\varepsilon_x$  (perpendicular to the loading direction) were evaluated after the test<sup>6–8</sup>.

The localization of deformation begins after reaching the maximum load. This phenomenon is allied with large deformation changes in the area of a slip band. Deformations were calculated using formula (1):

$$\varepsilon_y = \frac{dv}{dy} \quad (1)$$

where  $\varepsilon_y$  – deformation in longitudinal direction,  $v$  – displacement in direction Y (Y = direction of loading).

Deformation was evaluated by non-contact extensometry – videoextensometry. Deformation  $\varepsilon_y$  was measured between two dots. After the tensile tests the hardness HV 1 were measured in column 2 and column 6 (Fig. 2). Principle of UCI technique for hardness measuring is in Fig. 3. Relation between HV 1 and  $\varepsilon_y$  of steel IF is in Fig. 4. The relation between the hardness HV 1 and deformation is (2) ref.<sup>9</sup>:

$$HV1 = HV1_p + a\varepsilon^b \quad (2)$$

where  $HV1_p$  is the hardness of material before deformation;  $\varepsilon$  is tensile longitudinal deformation;  $a$ ,  $b$  are coeffi-

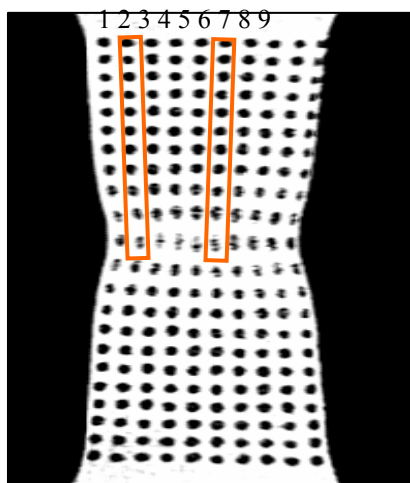


Fig. 2. Position of dots

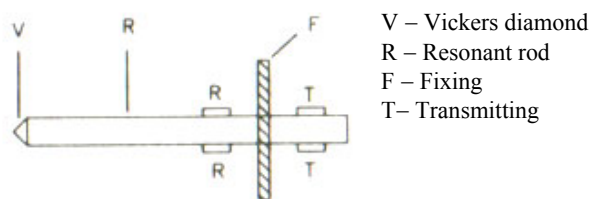


Fig. 3. Principle of UCI

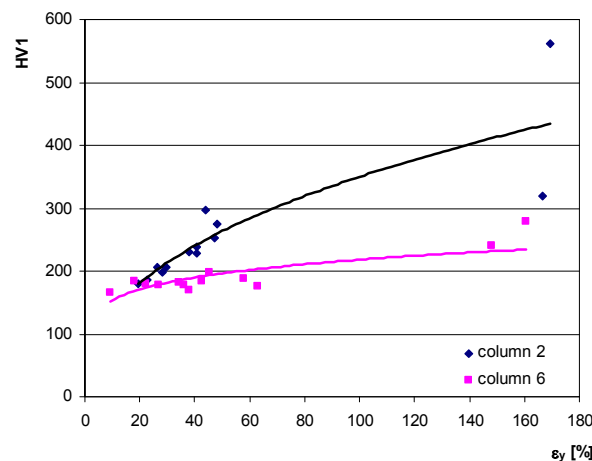


Fig. 4. Relation between HV1 and  $\varepsilon_y$  of IF steel

cients depending on the properties of the steels. The values of coefficients  $a$  are in order of  $10^1$ – $10^2$ . The values of coefficient  $b$  are in order of  $10^{-1}$  for all investigated steels. For steel IF the  $HV1_p = 110$ .

### 3. Conclusions

Using the videoextensometry and UCI technique enables to characterize the relation between the plastic deformation  $\varepsilon_y$  and hardness. The power relation between the hardness HV 1 and longitudinal deformation was applied. UCI is practical, portable experimental technique, appropriate to satisfactory determination of state of materials.

Measured values HV 1 are higher in column 2 near the edge of specimen. The stress conditions at the specimen edge and around the notch affect the hardening effect.

*This study was supported by the Grant Agency of Slovak Republic; grant project VEGA No. 1/4149/07 and APVV No. 0326-07.*

## REFERENCES

1. Lowe K.: Mater. World 2, 557 (1994).
2. Lis J., Lis A., Kolan K.: J. Mater. Process. Technol. 162, 350 (2005).
3. Bidulská J., Kvačkaj T., Bidulský R., Grande M.: Kovové materiály 46, 339 (2008).
4. Ohlsson C.: *International Workshop on Video – Controlled Materials Testing and In – situ Micro structural Characterization*, Nancy France, 89 (1999).
5. Pešek L.: *Lokální mechanické vlastnosti 2006*, (O. Bláhová, L. Pešek, ed.), p. 116. Plzeň – Nečtiny 2006.
6. Mihaliková M., Janek J.: Metalurgija 46, 107 (2007).
7. Sinn G., Reiterer A., Stanzl-Tschegg S. E., Tschegg E. K.: *Holz als Roh- und Werkstoff* 59, pp. 177–182. Springer-Verlag 2001.
8. Mihaliková M., Gazdag Š.: Metalurgija 47, 135 (2008).
9. Zubko P., Ambriško L., Pešek L.: *YUCOMAT 2009: Eleventh annual conference: Herceg Novi, Montenegro, August 31 – September 4, 2009*. Belgrade: Serbian Academy of Science & Arts, 2009. in print.

**M. Mihaliková, L. Ambriško, and L. Pešek**  
(*Department of material science, Faculty of metallurgy, Technical university of Košice, Slovakia*): **The Hardness Analysis of The IF Steel Sheet after a Plastic Deformation**

The paper deals with examination of relation between the hardness and deformation  $\varepsilon_y$ . UCI hardness method was used for hardness measurements. Deformation was evaluated by non-contact extensometry – videoextensometry. The results present existence of the power relation between hardness and plastic deformation:  $HV = HV_p + k\varepsilon^a$ .

## EVALUATION OF CARBON CONTENT IN AUSTENITE BY INDIRECT METHOD

**MÁRIA MOLNÁROVÁ<sup>a</sup>, TIBOR KVAČKAJ<sup>b\*</sup>, RÓBERT KOČIŠKO<sup>b</sup>, and LENKA NÉMETHOVÁ<sup>b</sup>**

<sup>a</sup> Institute of Materials Research, Slovak Academy of Sciences, 043 53 Košice, Slovakia, <sup>b</sup> Department of Metals Forming, Faculty of Metallurgy, Technical University of Košice, 042 00 Košice, Slovakia  
tibor.kvackaj@stuk.sk

Keywords: intercritical annealing, structure, microhardness, carbon content

### 1. Introduction

In the present time, marked demands for either a reduction of costs or a sensible increase in properties. The increase of properties can be obtained only through new innovation and/or new adapted solutions<sup>1–3</sup>.

Indirect method is based on fixation of austenite from experimental conditions by quick quenching to martensite. Authors<sup>4,5</sup> created a scheme of evolution of secondary phases during continuous cooling, see Fig. 1. Three types of hard phases created from austenite exist. Type 1 – hard boundary martensite, Type 2 – soft interior bainite, Type 3 – hard isolated martensite.

The interior austenite areas produce two types of secondary hard phases (Type 2 and 3) depending upon the

austenite grain size. If concentration of soluted carbon is high enough the stability of untransformed austenite increases and can result in formation of residual austenite.

The phase transformation from austenite must provide ferrite formation and saturation of austenite solid solution by carbon without possibility of pearlite and cementite formation. The pearlite formation can be suppressed by rapid cooling rate (cooling rate can not cross pearlite nose or cross pearlite zone in short time) and elements addition like Cr or Mn suppressing austenite transformation to pearlite at temperatures of 600–700 °C. The carbides formation and cementite precipitation formation are suppressed by adding Si, Al and P (ref.<sup>6–8</sup>). More ferrite content after intercritical annealing, means more retained austenite supersaturated by carbon diffused from bainitic ferrite after austempering. It can be described as a process in which the part of the austenite transforms to bainite, whereas retained austenite may become stabilized by carbon from bainitic ferrite but not transform to martensite during the final quenching to room temperature<sup>9</sup>.

This paper is aimed to evaluation of the carbon content in austenite by so called indirect method using microhardness measurement by Vickers method.

### 2. Experimental material and methods

Steel based on C-Mn-Si was investigated for the evolution of carbon content in austenite by indirect method based on microhardness measurement of martensite after scheme in Fig. 2, consisting of the controlled rolling and

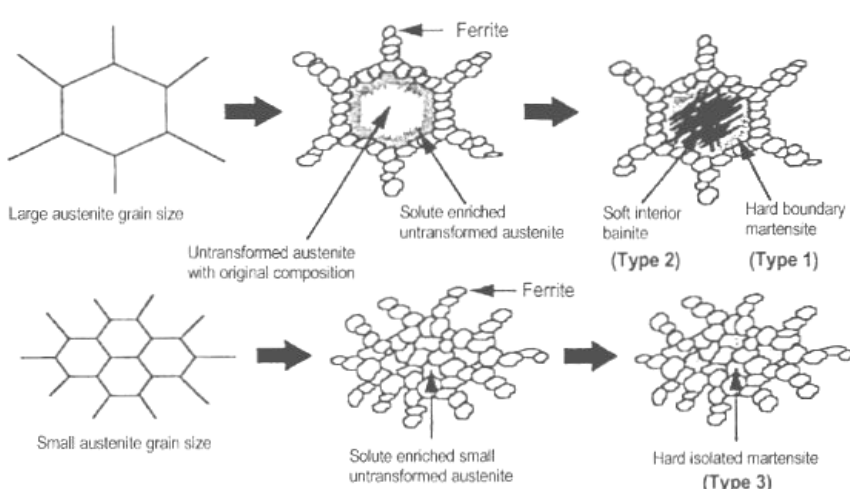


Fig. 1. Classification of hard second phase structures during continuous cooling<sup>4,5</sup>

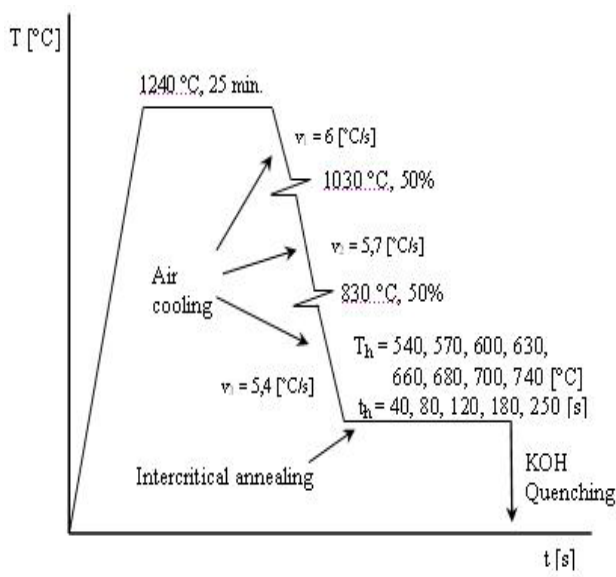


Fig. 2. Scheme for laboratory rolling and controlled cooling

controlled cooling process, included two step deformation (each 50 %). Intercritical annealing was held in temperature interval from 540 °C to 740 °C, with holding times from 40 to 250 s. Local chemical composition of the steel is in Tab. I.

Indirect method is based on fixation of austenite from experimental conditions by quick quenching to martensite. Carbon content was evaluated through the microhardness measurement (HV 0,05) by Vickers method. The data measured were converted into HV hardness values and carbon content in martensite was determined according to the equations published by<sup>10,11</sup>.

Microhardness was evaluated from about 30 indentations on each from selected samples and average values were used for equations (1–3) (ref.<sup>10,11</sup>):

$$HV = 0,75 HV_{0,05} \quad (1)$$

$$HV = 812 C + 293 \quad (2)$$

$$HV = 930 C + 283 \quad (3)$$

where C [wt.-%] is the carbon content in martensite and/or in austenite.

### 3. Results and discussion

The experimental results of carbon content in satu-

Table II  
Measured and calculated experimental data

Sample	Intercritical annealing	X <sub>F</sub> [%]	HV 0,05	HV	C <sub>Mart.</sub> [wt.-%]
1	670 °C / 120 s	24	724	543	0,28
2	620 °C / 120 s	39	810	608	0,35
3	700 °C / 180 s	32	763	572	0,31
4	700 °C / 240 s	32	749	562	0,30
5	740 °C / 180 s	18	637	478	0,21
6	570 °C / 180 s	62 +1%P	795	596	0,34
7	540 °C / 180 s	51 +30%P	700	525	0,26
8	570 °C / 80 s	49	759	569	0,307
9	740 °C / 40 s	7,5	677	508	0,242
10	660 °C / 40 s	1	687	515	0,249

rated austenite are given in Tab. II. Subsequently the experimental data were treated by linear statistics method and a regression equation was derived:

$$\% C_{\gamma} = -29,2 / (\% F - 132,3) \quad (4)$$

where F [%] is ferrite fraction in microstructure.

Fig. 3 shows the dependences of carbon content on ferrite fraction in saturated austenite for experimental C-Mn-Si steel (TRIP) and comparison with dual phase (DP) steel according to author<sup>12</sup>.

As it can be seen in Fig. 3, the experimental results of carbon content in austenite for C-Mn-Si steel (TRIP) refer to the higher values than for compared DP steel. Equilibrium value is 0,18 % C in austenite. Calculated values for carbon content in saturated solid solution of stabilized austenite were C = 0,21–0,35 % with dependence on ferrite fraction.

The curve course of carbon values is the same for the compared steel types, even though values for TRIP are higher for specific ferrite fractions (X<sub>F</sub> [%]). Also, the curve course is not so rapid, as for the DP steel.

The presence of silicon in steel 1,8 % Si combined with laboratory rolling and controlled cooling leads to ferrite and austenite formation and caused the carbon dif-

Table I  
Local chemical composition of C-Mn-Si steel [wt.-%]

Steel	C	Mn	Si	P	S	Cu	Ni	Cr	Al <sub>tot.</sub>	Nb	Sn
C-Mn-Si	0,18	1,47	1,8	0,015	0,007	0,06	0,04	0,06	0,028	0,005	0,007

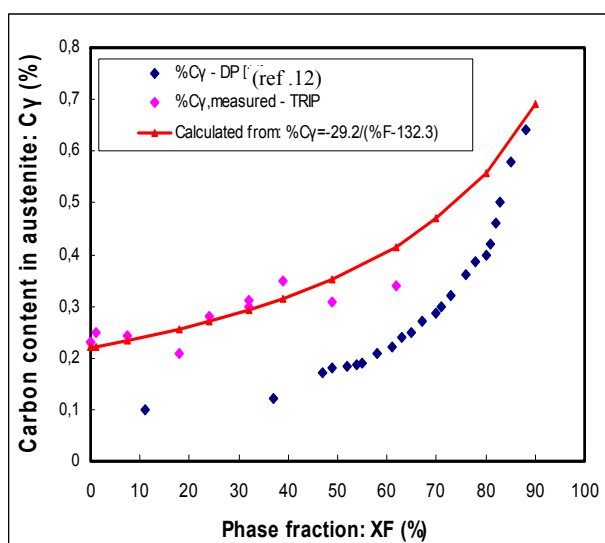


Fig. 3. Dependence of carbon content in austenite on ferrite fraction<sup>6</sup>

fusion from ferrite areas into austenite. Due to this austenite stabilization and saturation by carbon over the equilibrium value occurs.

Mechanical properties were influenced by the final structure, that after intercritical annealing consisted of ferrite, some mixture of bainite / martensite, and in some cases also pearlite. Intercritical annealed samples were quenched into KOH water solution, and mechanical properties were carried out by means of static tensile test. Yield strength  $R_{p0,2}$  and tensile strength  $R_m$  of air cooled samples reached values from 510 to 898 MPa and from 1052 to 1457 MPa.

#### 4. Conclusions

- The indirect method for evaluation of carbon content in saturated solid solution of stabilized austenite was used based on microhardness measurement of martensite.
- Calculated values of carbon content in austenite were 0,21–0,35 %, whereas the equilibrium value is 0,18 %C.
- Compared with results from author<sup>12</sup> for DP steels, carbon content for investigated TRIP steel refer to higher values for specific ferrite fractions.

This work was supported by the Scientific Grant Agency of Slovak republic as a grant project VEGA No. 2 / 7195 / 27.

#### REFERENCES

1. Pernis R., Bidulská J.: Manufact. Eng. 7, 17 (2008).
2. Bidulská J., Pokorný I.: Manufact. Eng. 7, 39 (2008).
3. Bidulský R., Actis Grande M.: High Temp. Mater. Process. 27, 249 (2008).
4. Kvackaj T., Molnárova M., Mišicko R., Fujda M.: *14<sup>th</sup> International Scientific Conference on Plasticity of Materials, Podbanské, Slovakia*, 181 (2007).
5. Park S.H., Choo W.Y., in: *Hot workability of steel and light alloy composites*, p. 493. Montreal, Canada, 1996.
6. Kvackaj T., Molnárova M., Mišicko R., Kočíško R., Bidulská J.: *15<sup>th</sup> International Conference on the Strength of Materials, Dresden*, Germany, 136 (2009).
7. Black W.: *International Conference on TRIP aided high strength ferrous alloy, Gent, Belgium*, 13 (2002).
8. Elsner A.: *Advanced hot rolling strategies for IF and TRIP steels*, Delft University Press, The Netherlands, 2005.
9. Jiang H., Wu H., Tang D., Qiang L.: J. of Univ. of Sci. and Techn. Beijing 15, 574 (2008).
10. Terasaki T., Akiyama S., Serino M.: *International Conference JOM-2*, 381 (1984).
11. Bernasovský P. et al.: *Náuka o materiáli a zvariteľnosť oceli*. Weldtech, Bratislava 1996.
12. Waterschoot T., De Cooman B. C., Vanderschueren D., Staelens B.: *Thermomechanical processing of steels*, p. 407. IOM Communications, London 2000.

**M. Molnárová<sup>a</sup>, T. Kvackaj<sup>b</sup>, R. Kočíško<sup>b</sup>, and L. Némethová<sup>b</sup>** (<sup>a</sup>Institute of materials research, Slovak academy of sciences, Košice, Slovakia, <sup>b</sup>Department of Metals Forming, Faculty of Metallurgy, Technical University of Košice, Slovakia): Evaluation of Carbon Content in Austenite by Indirect Method

The main aim of this paper was to evaluate the carbon content in austenite by so called indirect method using microhardness measurement by Vickers method. Indirect method is based on fixation of austenite from experimental conditions by quick quenching to martensite. Carbon content in saturated solid solution of stabilized austenite was  $C_y = 0,21\text{--}0,35\%$ , whereas equilibrium value in austenite is 0,18 %. This over-equilibrium carbon value is caused by increased silicon content in steel  $Si = 1,8\%$ .

## EXPERIMENTAL BACKGROUND FOR DIFFUSION MODELS OF Zr1Nb-O SYSTEM

**MARTIN NÉGYESI<sup>a</sup>, OLGA BLÁHOVÁ<sup>b</sup>,  
JAROSLAV BURDA<sup>c</sup>, and VĚRA  
VRTÍLKOVÁ<sup>d\*</sup>**

<sup>a</sup> Czech Technical University in Prague, FNSPE, DM Trojanova 13, 120 00 Praha 2, <sup>b</sup> New Technologies Research Centre, University of West Bohemia, Univerzitní 8, 306 14 Plzeň, <sup>c</sup> NRI Řež a.s., Husinec-Řež 130, 250 68 Řež, <sup>d</sup> UJP Praha a.s., Nad Kamínkou 1345, 156 10 Praha – Zbraslav, Czech Republic  
vrtilkova@ujp.cz

Keywords: Zr1Nb, oxygen concentration, nanohardness, pseudobinary phase diagram Zr1Nb-O

### 1. Introduction

The Zr1Nb alloy is used as a material for fabrication of nuclear fuel cladding tubes, which are the first barrier between the nuclear fuel and surroundings in the nuclear reactor. They lose their mechanical properties during operating conditions and especially after the hypothetical LOCA (Loss of Coolant Accident), because of oxidation, the oxygen and hydrogen uptake, a thermal shock and radiation damage. The oxygen and hydrogen uptake have the worst influence on the mechanical properties<sup>1–3</sup>. It is necessary to ensure that the reactor core integrity and cooling possibility, claddings' thermal shock resistance and the consequential materials handling during transport from the reactor is maintained even after the hypothetical LOCA. Many criteria based on claddings' mechanical properties after the simulated LOCA have been set up so far<sup>4,5</sup>. It should be noted that those high-temperature tests on unirradiated pre-corroded fuel claddings have the same predictive value as in case of high-temperature tests with long-term in-reactor exposure fuel claddings due to fact that the material damage is annealed during the heating process before the phase transformation  $\alpha\text{-Zr} \rightarrow \beta\text{-Zr}$ <sup>6</sup>. Nowadays there is an effort to create a universal criterion, applicable to any type of zirconium alloy, a cladding with any wall thickness and any number of fuel cycles (any corrosion thickness and any hydrogen content). That is why it is necessary to know the oxygen distribution (the microstructure) inside the fuel cladding's wall after the thermal transient. There is a picture of the cross section in Fig. 1 with a typical microstructure inside the wall of Zr-alloy fuel cladding after a transient. Upon the transient there is the phase transformation  $\alpha\text{-Zr} \rightarrow \beta\text{-Zr}$  inside the cladding and at the same time the oxygen stabilized  $\alpha\text{-Zr(O)}$  layer rises under the oxide layer, because of the oxygen uptake. After

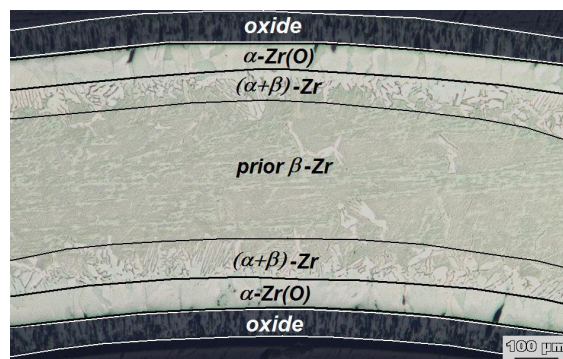


Fig. 1. A typical microstructure inside the wall of Zr1Nb fuel cladding - the 1200 °C/ 9 min sample

the cooling-down the wall microstructure consists of three layers: the oxide layer, the oxygen stabilized  $\alpha\text{-Zr(O)}$  layer and prior  $\beta\text{-Zr}$  layer, which is actually the Zr-alloy  $\alpha$ -phase transformed from the high-temperature Zr-alloy  $\beta$ -phase during the cooling<sup>7</sup>. In case of the Zr1Nb alloy there is a mixture of  $\alpha\text{-Zr(O)}$  and prior  $\beta\text{-Zr}$  between the oxygen stabilized  $\alpha\text{-Zr(O)}$  layer and prior  $\beta\text{-Zr}$  layer, because of the  $\beta$ -stabilizing effect of niobium<sup>8</sup>. In this paper the region is marked as  $(\alpha+\beta)\text{-Zr}$ .

### 2. Experimental

All specimens used in this study were made from the Zr1Nb alloy (Zr-1.0Nb-0.035Fe-0.135O, all in wt. %). Only as-received specimens were used. 30 mm long tubes (outside diameter 10 mm, wall thickness 686  $\mu\text{m}$ ) were exposed in a steam (0.1 MPa) at high temperatures (900–1200 °C) for variable time intervals in the resistance furnace CLASIC. The specimens' temperature was measured with a thermocouple inside the tube. After the high-temperature steam oxidation the specimens were quenched into water with ice. For nanohardness measurements and X-ray microanalysis polished cross sections were used.

Nanohardness measurements were carried out on a Nano Indenter XP (MTS System Corp. USA) with Berkovich indenter. The force was induced by a 0.8 g weight, so the indentation surface projection was about 0.5–2  $\mu\text{m}^2$  and the indentation depth was < 500 nm.

A wavelength-dispersive spectrometer INCA Wave 700, fully focusing six-crystal spectrometer Johansson (Oxford Instruments) was used for the oxygen concentration determination. A surface oxide layer was

removed from specimens. Specimens were polished with an OP-S suspension of colloidal silicate (Struers) and aluminized ( $\sim 15$  nm).  $\text{SiO}_2$  as a standard and LSM80N with the resolution FWHM 17 eV as a crystal were used for oxygen analyses.

### 3. Results and discussions

Nanohardness measurements were carried out in a few series perpendicular to the oxide/alloy interface leading over the  $\alpha\text{-Zr(O)}$  layer (showing a linear decrease of measured values) and the region  $(\alpha+\beta)\text{-Zr}$  (showing an experimental scatter increase and a decrease of the gradient) towards the middle of the cladding's wall – the prior  $\beta\text{-Zr}$  region with constant nanohardness values (Fig. 2). A nanohardness increase in the prior  $\beta\text{-Zr}$  region corresponds to a  $\alpha\text{-Zr(O)}$  grain. Distances between each indentation were 5  $\mu\text{m}$ . The measurement of the oxygen concen-

tration was carried out similarly. In both cases the measured values come from a volume of a few  $\mu\text{m}^3$ . A link between the measured nanohardness and oxygen concentration can be seen in Fig. 2. The nanohardness mainly depends on the oxygen concentration in the alloy. The experimental scatter of nanohardness values is caused mainly by the state of the sample surface.

There are also linear regression lines (a simplification: a linear decrease was supposed) with their equations and 95 % confidence intervals, which defines the area, in which the real regression line lies to 95 %, in Fig. 2. It is difficult to determine the exact values of the nanohardness and oxygen concentration at the  $\alpha/\alpha+\beta$  phase boundary, because this boundary is non-uniform in the Zr1Nb alloy. The following rules were used:

- A steep decrease of nanohardness/oxygen concentrations to the values equal to measured prior  $\beta\text{-Zr}$  values indicates the two-phase region  $(\alpha+\beta)\text{-Zr}$ .
- Nanohardness/oxygen concentrations at the  $\alpha/\alpha+\beta$  phase boundary must not be lower than values measured in the region  $(\alpha+\beta)\text{-Zr}$  and prior  $\beta\text{-Zr}$ .

In addition, for the determining of oxygen concentrations at the  $\alpha/\alpha+\beta$  phase boundary the niobium concentration profiles, which were measured together with the oxygen, could be used. The niobium is  $\beta$ -stabilizer, so there are locations containing more than 1 wt. % (a nominal content) of niobium in front of the  $\alpha\text{-Zr(O)}$  layer (Fig. 2). These locations can also rise inside the  $\alpha\text{-Zr(O)}$  layer, because the niobium has low diffusivity in zirconium cell.

The oxygen concentration at the  $\alpha/\alpha+\beta$  phase boundary is determined by linear regression methods (come from one specimen only) and the nanohardness at the boundary is a mean value, because of larger amount of experimental results. The nanohardness measurement is less time-consuming compared to WDS, which is great advantage. Nanohardness and oxygen concentrations at the  $\alpha/\alpha+\beta$  phase boundary rise with rising exposition temperature (Fig. 3, 4). The whole oxygen concentration profile at the specimen exposed to 950 °C temperature was systematically lower. The nanohardness measurement of the specimens exposed to the 1,050 °C may also have a systematic error (e.g. poorly prepared surface). There are also nanohardness and oxygen concentrations at the  $\alpha/\alpha+\beta$  phase boundary in the cladding wall from the Zry-4 alloy ( $\text{Zr-(1.3-1.5)Sn-0.2Fe-0.1Cr-0.12O}$ , all in wt. %) with various amount of hydrogen, for comparison in Fig. 3 and 4. The results are adopted from earlier work<sup>9</sup>. The hydrogen ( $\beta$ -stabilizer) causes an oxygen concentration and also nanohardness increase at the  $\alpha/\alpha+\beta$  phase boundary in the cladding wall from the Zry-4 alloy<sup>5,9</sup>. It is therefore likely that niobium will have the similar effect. Nanohardness and oxygen concentrations at the  $\alpha/\alpha+\beta$  phase boundary in the cladding wall from the Zr1Nb alloy are similar to nanohardness and oxygen concentrations at the  $\alpha/\alpha+\beta$  phase boundary in the cladding wall from the Zry-4 alloy with high hydrogen content ( $> 2000$  wppm). Fig. 4 shows the comparison of WDS results with the Zry-4-O pseudobi-

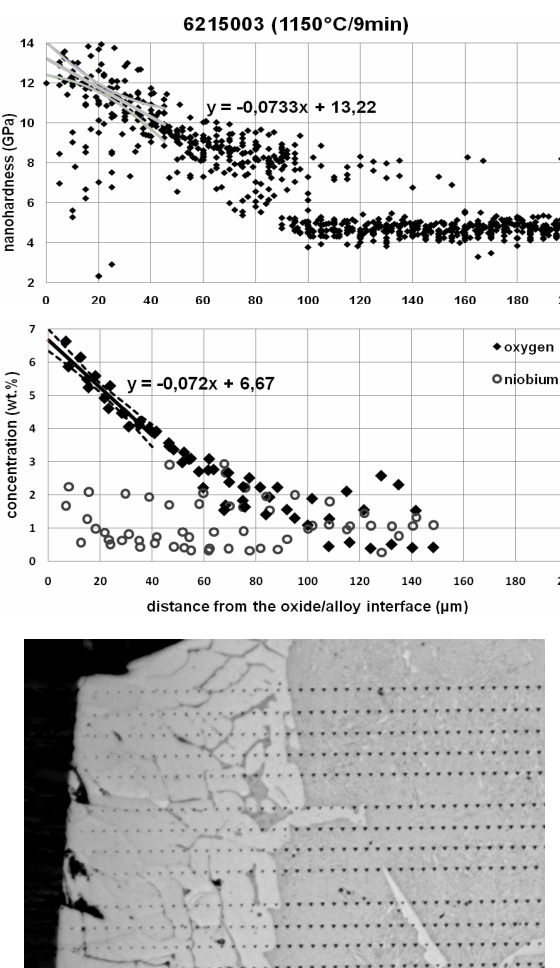


Fig. 2. Nanohardness and oxygen concentration profiles and an image of nanoindentation series - the 1150 °C/ 9 min sample

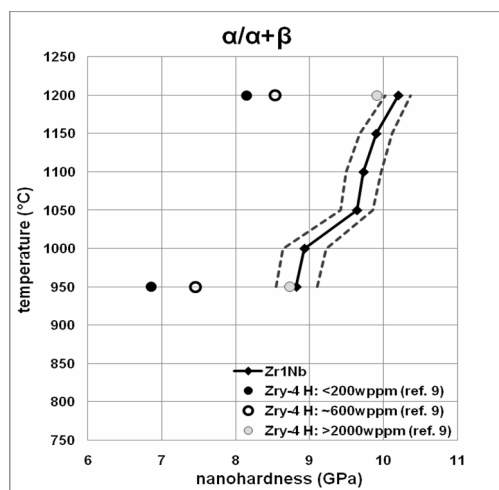


Fig. 3. Nanohardness at the  $\alpha/\alpha+\beta$  phase boundary in the cladding's wall from the Zr1Nb and Zry-4 alloys with various hydrogen content

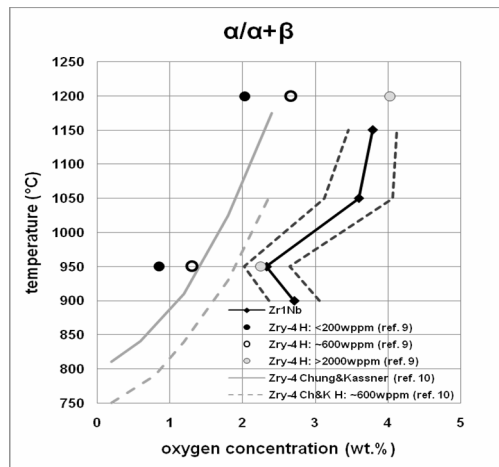


Fig. 4. Oxygen concentrations at the  $\alpha/\alpha+\beta$  phase boundary in the cladding's wall from the Zr1Nb and Zry-4 alloys with various hydrogen content

nary phase diagram<sup>10</sup>. The present results for the Zry-4 alloy are systematically lower. Dashed curves in both graphs are constructed using the 95 % confidence intervals. They define the region, in which the real boundary line  $\alpha/\alpha+\beta$  lies to 95 % (without any consideration of measurement errors).

In an earlier work<sup>9</sup> a relation between the nanohardness and oxygen concentration at the  $\alpha/\alpha+\beta$  phase boundary in the cladding wall from the Zry-4 alloy was determined. The results come from the alloy Zr1Nb confirm this relation (Fig. 5). The relation is extended to the point [6.82:12.5] – the oxygen concentration and nanohardness at the oxide/alloy phase boundary. The nanohardness value (12.5 GPa) is the average value of all measured samples

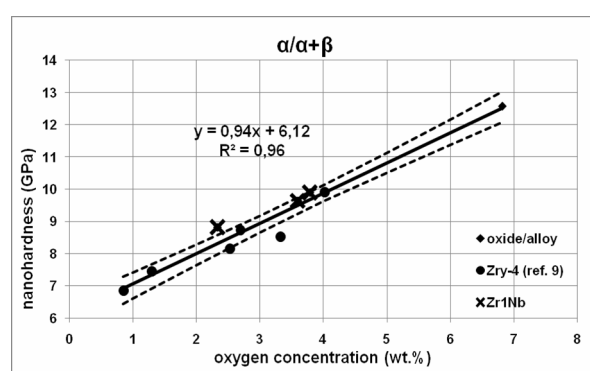


Fig. 5. The relation between the nanohardness and oxygen concentration at the  $\alpha/\alpha+\beta$  phase boundary

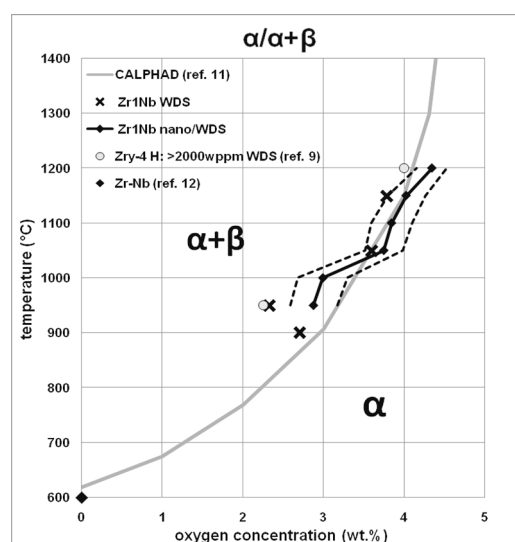


Fig. 6. A part of the Zr1Nb-O pseudobinary phase diagram determined by nanoindentation and WDS methods and computed by the method CALPHAD

and the oxygen concentration (6.82 wt. %) is the average value of oxygen concentrations at the temperatures 950 and 1200 °C come from the Zr-O equilibrium phase diagram. There is also the linear regression line with its equation and 95 % confidence interval in Fig. 5. The relation is equally valid for both alloys.

Using the relation above oxygen concentrations at the  $\alpha/\alpha+\beta$  phase boundary can be determined indirectly from nanohardness values. Such determined oxygen concentrations are together with oxygen concentrations determined by WDS are shown in Fig. 6. Dashed curves define the region, in which the real boundary line  $\alpha/\alpha+\beta$  lies to 95 % (without any consideration of measurement errors). Assuming local equilibrium conditions at the phase boundaries in the exposed cladding, the oxygen concentrations at the phase boundaries can be considered equilibrium. So

the oxygen concentrations measured at the  $\alpha/\alpha+\beta$  phase boundary can be used to construct a part of the Zr1Nb-O pseudobinary phase diagram. There are also oxygen concentrations at the  $\alpha/\alpha+\beta$  phase boundary in the cladding wall from the Zry-4 alloy with high hydrogen content ( $> 2,000$  wppm) for a comparison in Fig. 6. Very good agreement with the calculation CALPHAD<sup>11</sup> has been obtained. The point corresponding to the zero oxygen concentration comes from the Zr-Nb equilibrium phase diagram<sup>12</sup>.

A part of the Zr1Nb-O pseudobinary phase diagram (the interface  $\alpha/\alpha+\beta$ ) has been estimated using exposed fuel claddings by methods WDS and nanohardness measurements. Such way a pseudobinary phase diagram of the Zr-alloy-O system up to a few units wt. % could be constructed. This is unavailable by conventional methods such as dilatometry, calorimetry, etc., because specimens are very brittle.

#### 4. Conclusions

The aim of this work was to determine the nanohardness and oxygen concentration at the  $\alpha/\alpha+\beta$  phase boundary in the cladding wall of exposed specimen from the Zr1Nb alloy by nanoindentation and WDS methods and to try to use these results to the construction of the Zr1Nb-O pseudobinary phase diagram. The conclusions:

- Oxygen concentrations and also nanohardness at the  $\alpha/\alpha+\beta$  phase boundary in the cladding from the Zr1Nb alloy rise with rising exposition temperature and are similar to oxygen concentrations and nanohardness at the  $\alpha/\alpha+\beta$  phase boundary in the cladding from the Zry-4 alloy with hydrogen content  $> 2,000$  wppm.
- The relation between the nanohardness and oxygen concentration at the  $\alpha/\alpha+\beta$  phase boundary in the phase  $\alpha\text{-Zr(O)}$  for the temperature range 950–1200 °C has been assessed. The relation is equally valid for both alloys.
- The part of the Zr1Nb-O pseudobinary phase diagram (the interface  $\alpha/\alpha+\beta$ ) has been estimated by WDS methods and nanohardness measurement using exposed fuel claddings.

For more exact determination of the Zr1Nb-O pseudobinary phase diagram it is required to have more experimental results, especially results of time-consuming WDS measurements. Using the relation between the nanohardness and oxygen concentration at the  $\alpha/\alpha+\beta$  phase boundary the oxygen concentrations can be determined indirectly from the nanohardness values.

*Authors wish to thank Mr. L. Novotný, J. Šustr and A. Přibyl for the samples and metallographic scratch patterns and S. Linhart for English correction. This work was supported by "PROJEKT MPO 2A-ITP1/037".*

#### REFERENCES

1. Billone M., Yan Y., Burtseva T., Daum R.: Research report NUREG/CR-6967. ANL, Argonne 2008.
2. Grandjean C., Hache G.: Research report DPAM/SEMCA 2008-093. IRSN, 2008.
3. Stern A. et al.: J. ASTM Int. 4, 1 (2007).
4. Chung H. M., Kassner T. F.: Research report NUREG/CR-1344 ANL-79-48. ANL, Argonne 1980.
5. Chung H. M.: Nucl. Eng. Tech. 37, 327 (2005).
6. Portier L. et al.: J. ASTM Int. 2, 103 (2005).
7. Brachet J.C. et al.: Research report DEN/DMN/SRMA 91191. CEA, Saclay.
8. Vrtílková V. aj.: Research report UJP 1313. UJP, Praha 2008.
9. Négyesi M.: Research report. ČVUT-FJFI-KMAT, Praha 2008.
10. Chung H. M., Kassner T. F.: J. Nucl. Mat. 84, 327 (1979).
11. Sopoušek J.: Research report. MU PF, Brno 2009.
12. Okamoto H.: J. Phase Equil. 13, 577 (1992).

**M. Négyesi<sup>a</sup>, O. Bláhová<sup>b</sup>, J. Burda<sup>c</sup>, V. Vrtílková<sup>d</sup>**  
<sup>a</sup>Czech Technical University in Prague, <sup>b</sup>New Technologies Research Centre, University of West Bohemia, <sup>c</sup>NRI Rež a.s., <sup>d</sup>UJP Praha a.s., Czech Republik: **Experimental Background for Diffusion Models of Zr1Nb-O System**

A pseudobinary phase diagram of the Zr1Nb-O system, acceptable for diffusion models predicting the behavior of Zr1Nb fuel claddings during transients, has not been still published. This work is the contribution for this problem solving. The determined oxygen concentrations at the phase boundaries in the wall of fuel claddings exposed in a steam have been used for the phase diagram assessment. In this study oxygen concentrations at the  $\alpha/\alpha+\beta$  phase boundary in the phase  $\alpha\text{-Zr(O)}$  have been determined base on results of WDS and nanoindentation measurements. The relation between the nanohardness and oxygen concentration at the  $\alpha/\alpha+\beta$  phase boundary in the phase  $\alpha\text{-Zr(O)}$  has been assessed.